POLITECNICO DI TORINO
Repository ISTITUZIONALE

Molybdenum/Niobium Disilicide Multilayers Fabricated by Tape Casting: Microstructure, Mechanical Properties and Oxidation Behaviour

Original
Molybdenum/Niobium Disilicide Multilayers Fabricated by Tape Casting: Microstructure, Mechanical Properties and Oxidation Behaviour / Vásquez, D.M., Padovano, E., Badini, C., Biamino, S., Lavagna, L., Pavese, M.. - In: MATERIALS. - ISSN 1996-1944. - ELETTRONICO. - 19:8(2026), pp. 1-24. [10.3390/ma19081653]

Availability:
This version is available at: 11583/3010520 since: 2026-05-04T10:40:15Z

Publisher:
MDPI

Published
DOI:10.3390/ma19081653

Terms of use:

This article is made available under terms and conditions as specified in the corresponding bibliographic description in the repository

Publisher copyright

(Article begins on next page)

18 November 2026

materials

MDPI

Article

Molybdenum/Niobium Disilicide Multilayers Fabricated by Tape Casting: Microstructure, Mechanical Properties and Oxidation Behaviour

Dreidy Mercedes Vásquez [1,2], Elisa Padovano [1], Claudio Badini [1], Sara Biamino [1], Luca Lavagna [1] and Matteo Pavese [1,*]

[1] Department of Applied Science and Technology, Politecnico di Torino, Corso Duca degli Abruzzi 24, 10129 Torino, Italy; dreidy.vasquez@pucv.cl (D.M.V.); elisa.padovano@polito.it (E.P.); claudio.badini@polito.it (C.B.); sara.biamino@polito.it (S.B.); luca.lavagna@polito.it (L.L.)

[2] Escuela de Ingeniería Química, Pontificia Universidad Católica de Valparaíso, Av. Brasil 2950, Valparaíso 2362854, Chile

* Correspondence: matteo.pavese@polito.it

Abstract

$MoSi_2$-based intermetallics are interesting materials for high-temperature applications, due to their moderate density, high melting point and significant oxidation resistance. In this paper, $MoSi_2$-based materials in the form of multi-layered structures were fabricated by tape casting and pressureless sintering. Composites containing up to 20 wt.% of $NbSi_2$ were produced, with the aim of obtaining biphasic structures with low pest oxidation at low temperature. The prepared samples were characterised with regard to phase composition, microstructure, mechanical properties and oxidation resistance. It was shown that the addition of a limited amount of $NbSi_2$ prevents the pest oxidation phenomenon characteristic of pure $MoSi_2$. Silica inclusions responsible for lowering the material toughness, were observed to disappear in the sintered silicides, thanks to the presence, during the binder burn-out, of a reducing atmosphere and to the carbonaceous residua. The phase and composition analysis also revealed the formation of small amounts of secondary phases like silicon carbide.

Keywords: molybdenum silicide; niobium silicide; tape casting; mechanical properties; oxidation resistance

1. Introduction

The study of intermetallics is becoming more and more important because of the higher demand of aerospace and microelectronics industries for materials that can operate at higher temperature and with a better mechanical and chemical performance than currents alloys (e.g., nickel-based alloys, see for instance [1,2]). The interest is focused on the development of new materials with characteristics such as good fracture toughness, creep and fatigue resistance combined with resistance to oxidation or to a corrosive environment, in particular at high temperature. The modification of known materials is thus required to allow this properties improvement [1–4].

$MoSi_2$-based materials are one of the possibilities currently envisaged in this field. Two main characteristics make molybdenum disilicide a potential material for use in applications subjected to severe thermal and corrosive environments: its high melting point (2030 °C) and its excellent oxidation resistance at high temperature, coupled with a relatively low density (6.20 g/cm^3), high Young's modulus at room temperature (440 GPa) and

Check for updates

Academic Editors: Shiwei Wu and Zixu Guo

Received: 13 February 2026
Revised: 13 April 2026
Accepted: 14 April 2026
Published: 21 April 2026

Copyright: © 2026 by the authors. Licensee MDPI, Basel, Switzerland. This article is an open access article distributed under the terms and conditions of the Creative Commons Attribution (CC BY) license.

good thermal and electrical conductivity [5–7]. Its good thermal conductivity also suggests applications where an effective cooling of the products is needed, like engine components, substituting a forced cooling system [8]. Another interesting property of molybdenum silicide is its limited thermal expansion coefficient, between 8 and $10 \cdot 10^{-6}$ K^{-1} from room temperature to 1400 °C [8].

$MoSi_2$ is, however, a rather brittle compound. Its fracture toughness at room temperature is around 2–3 MPa $m^{1/2}$, even if some papers report it to be up to 5 MPa $m^{1/2}$ [9], depending of the testing technique used. Moreover, it has a brittle-to-ductile transition at high temperature (over 1000 °C) and both tensile strength and creep resistance decrease substantially with the increase in temperature over the brittle-to-ductile transition [10]. Apart from the inherent brittleness of the intermetallic compounds, another cause of low toughness of this compound is the presence of silica inclusions in the sintered parts [3–7]. Silica forms on the surface of the powders during their synthesis, and during the sintering step it segregates inside the material with the formation of inclusions that generate brittleness and worsen oxidation resistance.

At high temperature, $MoSi_2$ presents an outstanding oxidation resistance, thanks to the formation of a dense SiO_2 glassy film, which protects the underlying material from further oxidation. However, at intermediate temperatures, a phenomenon reported as "pest oxidation" occurs [11–15]. This is due to the formation of molybdenum oxide, following the equation:

$$2\ MoSi_2(s) + 7\ O_2(g) \rightarrow 2\ MoO_3(s) + 4\ SiO_2(s) \quad (1)$$

Molybdenum oxide forms at rather low temperatures (400–800 °C), but then it melts and starts evaporating, between 800 and 1200 °C, so that no passivation can occur. Only over 1200 °C does the oxidation follow a passivating route, since no molybdenum oxide forms, through the equation:

$$5\ MoSi_2(s) + 7\ O_2(g) \rightarrow Mo_5Si_3(s) + 7\ SiO_2(s) \quad (2)$$

Pest oxidation is favoured due to the presence of flaws inside the material, such as pores, internal cracks and SiO_2 inclusions.

Thus, to promote the application of $MoSi_2$ as a structural material in aerospace industry, it is necessary to improve both oxidation resistance and room temperature mechanical properties. In order to increase the mechanical properties of molybdenum disilicide, one of the possibilities is to use a second phase to modify the base material [16–18]. One of the promising candidates for this task is niobium disilicide, which presents similar thermal behaviour, high melting point and high strength at high temperature [19–32].

Another possible approach is to find a preparation technique for this compound that helps to improve the properties. The main preparation methods used for molybdenum disilicides are arc melting, mechanical alloying and combustion synthesis, even if other approaches are used, like shock synthesis, chemical vapour deposition or infiltration, reactive vapour infiltration and field-activated combustion synthesis [33–36]. For the consolidation of dense $MoSi_2$ components, many approaches have been applied [33], including hot pressing, hot isostatic pressing, plasma spray, rapid solidification rate, low-pressure plasma spraying, vacuum plasma spraying, spark plasma sintering and tape casting, which is the one used in this work. Most of them, however, are based on the application of pressure at high temperature and thus are less versatile than pressureless sintering methods.

In this paper, we propose the tape casting technique, followed by pressureless sintering, using $NbSi_2$ as a substitution of $MoSi_2$. Since the substitution amount is small, $NbSi_2$ acts almost as a sintering aid, but with the aim of improving oxidation resistance.

Tape casting is a method used to produce multilayer materials by the stacking of thin or thick layers [37–41]. The technique allows one to obtain parts with uniform density and homogeneous pore size distribution. It consists of preparing a well-dispersed suspension of ceramic powders, through the use of a dispersant agent, mixed with other organic components such as binders and plasticisers, and casting it on a polymeric support to obtain flat and thin sheets that are flexible and strong. The process is simple, industrially scalable and low-cost, and through a convenient stacking of single tapes, it is possible to produce components of various shapes and size. The most successful industrial use of this technique is in the electronic industry, and there is high potential in the fabrication of solid oxide full cells, amongst others.

In this paper, this technique is used because it can provide high strength to the prepared materials, as demonstrated by Biamino et al. [5], who successfully processed $MoSi_2$ using tape casting followed by pressureless sintering. This paper indicates that this process seems also to reduce the formation of oxide inclusions in the silicide intermetallic, improving both strength and oxidation resistance. By the introduction of weak or porous layers in the multilayered structure, tape casting may also allow improvements in the toughness through crack deflection and the consequent increase in the dissipated energy before fracture [42].

Molybdenum silicide multilayers were also studied by Zhang and co-workers [43], who obtained by hot-pressing complex multilayers systems consisting of a sandwich structure of Al_2O_3, TiC and $MoSi_2$ + Mo_2B_5 layers, where $MoSi_2$ + Mo_2B_5 showed superplastic behaviour. Tuffe et al. [44] proposed a $MoSi_2$–Al_2O_3 structure in which the multilayer was constructed by an internal part of pure $MoSi_2$ and an external one of a composite containing 25% of Al_2O_3. The material was obtained by hot pressing. Dumont and coworkers [45] proposed instead a $MoSi_2$–Al_2O_3 functionally graded material fabricated by tape casting and sintering by SHS, showing a gradient in electrical conductivity through the thickness. Roncari et al. [46] worked on the AlN–SiC–$MoSi_2$ system, obtaining densities of up to 94% after pressureless sintering aided by sintering aids, but showing no mechanical data. Chen et al. [47] used elemental powders of Mo, Si, and C and pressureless sintering, obtaining 93% density with a final content of 10% silicon carbide. Magnani et al. [15] instead used liquid infiltration of a porous preform to obtain a density higher than 92%. In these last cases, however, $MoSi_2$ is used in an unalloyed form, thus not addressing the issues related to its oxidation resistance. Jo and Shon [48] proposed a 50%$MoSi_2$–50%$NbSi_2$ nanostructured composite obtained by a pulsed current-activated synthesis and consolidation method. They obtained a duplex phase with good density but the only mechanical property considered is hardness, together with an estimation of toughness from crack length. Kang and Shon [49] prepared also a 50%$MoSi_2$–50%$NbSi_2$ composite by high-frequency induction heated sintering, with results very similar to the ones obtained by Jo and Shon.

Several other research groups have prepared $MoSi_2$-based composites: Zhang et al. [50] prepared a $MoSi_2$–CNT (carbon nanotube) composite by hot pressing, obtaining very good toughness for a 6% CNT content. A similar material was also recently realised by Nazari et al. [51]. More recently, Zhang et al. [52] prepared a $MoSi_2$–UHTC composite, using ZrB_2 and SiC, for heating element applications. For the same application, Wick-Joliat et al. [53] prepared a $MoSi_2$–Al_2O_3–feldspar composite by ceramic-injection moulding, but in this case, $MoSi_2$ was present only for providing conductivity, and the main component was the other ceramics. Feng et al. [54] produced some Si_3N_4–$MoSi_2$ composites with La_2O_3 and Y_2O_3 sintering aids by hot pressing, where the main contribution to strength was given, however, by the Si_3N_4 phase, while Titov et al. [55] used Si_3N_4 as an additive to improve low temperature oxidation of $MoSi_2$ obtained by hot pressing. More recently,

Demir et al. [56] realised a $MoSi_2$–MoB_2 composite with improved fracture toughness, and Huang et al. [57] a $MoSi_2/Al_2O_3$ composite with interesting strength. The most recent publication is by Bei et al. [58], who proposed a $MoSi_2$–MoAlB composite with high strength and toughness. In all these cases, the use of composite materials allowed improvements in toughness and strength.

Slightly different materials were prepared by Gao et al. [59], who produced some interesting $MoSi_2$–RSiC interpenetrating phase composites, albeit with low strength, while similar composites were produced by Xie et al. [60], using phenolic resin infiltration-pyrolysis and $MoSi_2$–Si–Ti alloy-activated melting infiltration. Silicon infiltration was used by Huang et al. [61] to produce dense $SiC_f/MoSi_2$ composites, but multiple impregnation–calcination cycles are needed to have a continuous $MoSi_2$ phase, and residual Si is present. Zhang et al. [62] too prepared a nano $MoSi_2$–SiC composite by melt infiltration of silicon.

Another interesting approach is also from Jain et al. [63], where laminated composites between $MoSi_2$/SiC and a metal (Mo, Ta, Nb) were realised. More recently, Kaledin et al. [64] fabricated layered SiC/C/Si/$MeSi_2$/Me composites via liquid silicon infiltration. Lu et al. [65,66] prepared $MoSi_2$–SiC composites by vacuum hot pressing, with good mechanical properties and improved pest oxidation resistance by pre-oxidation at 1200 °C of $MoSi_2$ containing Nb, Al and SiC. Monteverde et al. [67] prepared $MoSi_2$–ZrB_2 materials with dual composite architecture by hot pressing, while Pogozhev et al. [68] prepared ZrB_2–$ZrSi_2$–$MoSi_2$ and HfB_2–$HfSi_2$–$MoSi_2$ composites by magnesiothermic SHS and hot pressing. A similar technique was used by Gorshkov et al. [69] to produce (MoW)Si_2. Yeh and Peng [70] produced $MoSi_2$–Al_2O_3 with thermite-like reactions in a wide range of compositions, while Zaki et la. [71] used a similar reactive approach to obtain mullite/$MoSi_2$ composites.

Regarding oxidation resistance, Potanin [72] prepared $MoSi_2$–HfB_2–MoB composites, observing the formation of a borosilicate oxide surface layer and also of $HfSiO_4$, with good oxidation results. Borosilicate glass was used by Tao et al. [16] to guarantee self-healing ability to a $MoSi_2$/borosilicate glass composite. Vorotilo et al. [73,74] used $MoSi_2$–MoB composites obtained by SHS and hot pressing with the idea of limiting MoO_3 evaporation at medium temperature through the formation of a borosilicate glass. Yan et al. [75] also used boron (working in the Mo–Si–B system) to improve oxidation resistance in SPS composites, observing improved performance with increasing B content. Zhang et al. [76] prepared in situ $MoSi_2$-SiC-MoB composites with low pest oxidation but not optimal mechanical properties. Safaie et al. [77] added Al to consume SiO_2, while Silvestroni [78] studied the oxidation of SiC/$MoSi_2$ composites at ultra-high temperature. Recently, Huang et al. [79] suggested the use of WSi2 as an additive to $MoSi_2$ for improved oxidation resistance.

Several studies concern the use of $MoSi_2$-based composites as coatings for oxidation protection of C/C composites or Mo- or Nb-based alloys. Hu et al. [80] prepared $MoSi_2$–mullite coatings for C/C composites protection, while Chen et al. [81] prepared $MoSi_2$–SiC composites for graphite protection by using recycled $MoSi_2$ heating elements. Li et al. [82] prepared $MoSi_2$/(Mo,Ti)Si_2 dual-phase composites to protect Mo alloys, and finally, Bezzi et al. [83] developed SiC/$MoSi_2$ composites as C/C coatings. Recently, Zhu et al. [84] prepared a $MoSi_2$ coating with SiC whiskers for oxidation protection, while Zhang et al. [85] proposed the superposition of a pre-oxidised (Nb,X)Si_2 layer with a $MoSi_2$ coating to improve adhesion and oxidation resistance. An interesting approach was also proposed by Ji et al. [86], who used thermal expansion mismatch to design gradient coatings of ZrB_2, $MoSi_2$ and a borosilicate glass. In all these cases, the oxidation was performed at very high temperature, thus not considering the effect of pest oxidation. Zhai et al. [87] proposed a ZrB_2/SiC/$MoSi_2$ coating that exploited rapid oxidation at low temperature as a way to reduce pest oxidation issues.

This expansive literature suggests that the topic of $MoSi_2$-based composites is currently of great interest for the scientific community, and oxidation resistance remains one of the key factors to consider when studying these kinds of materials.

The aim of this paper was to study the oxidation resistance of $MoSi_2$-based materials when coupling the preparation by the tape-casting technique with the addition of small quantities of $NbSi_2$. The use of tape casting allows the elimination of silica inclusions, as observed in a previous paper of ours [5], thus improving oxidation resistance. The addition of $NbSi_2$ in small quantities (up to 20 wt.%) should guarantee a finer duplex microstructure. Phase composition, mechanical properties and oxidation resistance (at low and high temperature) were analysed for these composites.

2. Materials and Methods

The powders of molybdenum and niobium silicide were obtained by ABCR. The mean powder size for $MoSi_2$ was 2–3 μm, while the $NbSi_2$ powders were larger, with a wide distribution under 45 μm. In the powders, two impurities were observed: SiO_2 (on the surface) for both powders, and Mo_5Si_3 or Nb_5Si_3 for $MoSi_2$ and $NbSi_2$, respectively.

As discussed in the introduction, tape casting is a technique that involves the combination of different components into the slurry to provide a very well-mixed material for the fabrication of flat sheets. The flow chart of the preparation method is shown in Figure 1. The powders were dispersed in inorganic solvents by the addition of 0.1% fish oil and then mixed for 24 h in a ball mill. After the addition of binder and plasticiser, further mixing for 24 h was performed. The slurries were rheologically optimised in a preliminary step of the work, in order to obtain a viscosity and a rheological behaviour suitable for the subsequent casting step. The detailed composition of the slurry is given in Table 1. During the ball-milling step, air can be entrapped into the slurry, so that before casting, a step of vacuum degassing was performed, keeping the slurry in a vacuum chamber until no more bubbles were observed on the surface (around 15 min). The casting was carried out on a tape casting machine with a stationary doctor blade and a moving Mylar® carrier film. All the slurries were cast at 100 mm/min of speed and the blade gap was adjusted to 1 mm. The cast slurry was slowly dried in calm air at room temperature to eliminate the organic solvents, giving a flexible sheet of thickness around 200–250 μm.

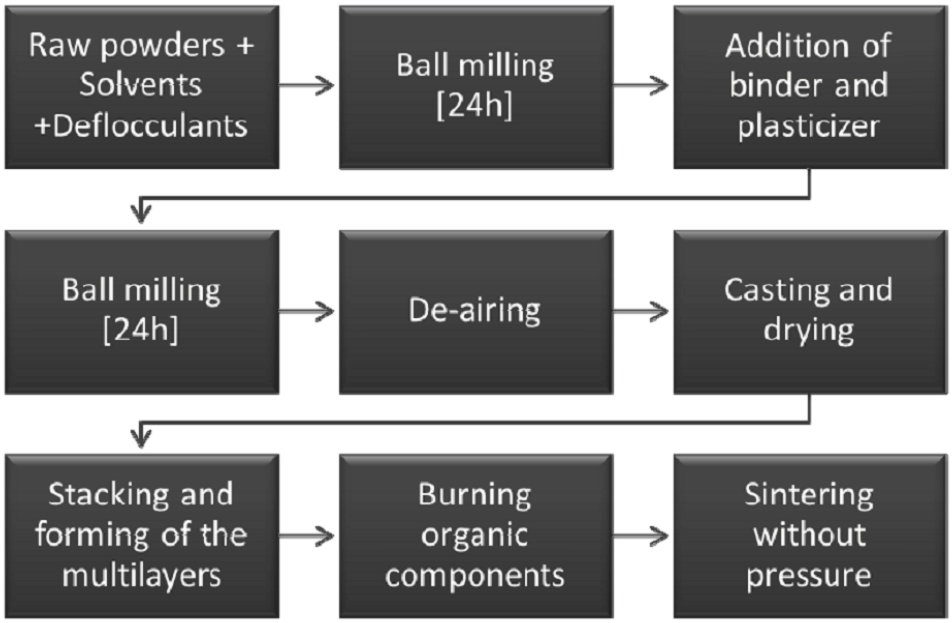


Figure 1. Flow chart of the preparation method of the multilayers by tape casting and pressureless sintering.

Table 1. Slurry composition for the different multilayers produced in the $MoSi_2$/$NbSi_2$ system.

Components		$MoSi_2$	5%$NbSi_2$	10%$NbSi_2$	20%$NbSi_2$	40%$NbSi_2$	50%$NbSi_2$	$NbSi_2$
wt. % $MoSi_2$		100	95	90	80	60	50	0
Solvents	Ethanol				14.8			
	Butanol				22.8			
Dispersant	Fish oil				0.1			
Powders	$MoSi_2$	51.4	48.8	46.3	41.1	30.8	25.7	0.0
	$NbSi_2$	0.0	2.6	5.1	10.3	20.6	25.7	51.4
Binder	Polyvinylbutyral				7.2			
Plasticiser	Polyethyleneglycol				3.7			

The multilayer samples were prepared by cutting the green dry tapes in rectangular pieces of 60 × 100 mm, and stacking the pieces one upon the other, making sure to put in contact a rough surface (the one in contact with the air during casting) with a smooth one (the one in contact with the Mylar support during casting). By using a glue and by rolling with a mandrel, every layer adhered perfectly to the underlying one, thus avoiding the formation of air bubbles between layers. The bond glue was prepared by mixing water, ethanol and polyvinyl alcohol (PVA). For every composition, eight multilayer samples of 60 × 12 mm with 10 layers were fabricated by cutting one 60 × 100 mm rectangular multilayer.

Binder, plasticiser and other additives were burned out by slow heating up to 800 °C in an Elite oven in a flowing argon atmosphere to prevent oxidation and to carry away the products of the decomposition of the organic substances. In order to determine the optimal heating rate for this step, the organics decomposition was studied by thermogravimetric experiments realised on dried tapes. A Mettler Toledo TGA/SDTA 851e (Greifensee, Switzerland) instrument was used, with a measurement accuracy of 0.5 K and a resolution of 1 μg. The thermal decomposition of a tape containing $MoSi_2$ powder in argon flow at the slow heating rate of 1 °C/min is depicted in Figure 2, together with the decomposition behaviour of tapes containing mixed $MoSi_2$–$NbSi_2$ powders (50%$MoSi_2$) or pure $NbSi_2$ powder. Most of the weight is lost between 200 and 400 °C, where the thermal decomposition of binder and plasticiser occurs. The difference in the decomposition profile of the tapes containing silicides of different Mo and Nb contents are not very significant, and can be probably ascribed to a catalytic effect of the metals on the decomposition kinetics.

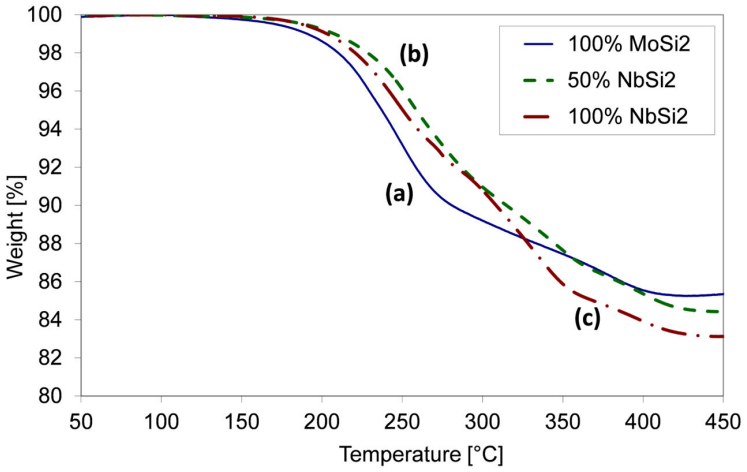


Figure 2. Thermogravimetric curves, under argon flow at the heating rate of 1 °C/min, of tapes containing: (a) 100%$MoSi_2$, (b) 50%$MoSi_2$–50%$NbSi_2$, (c) 100%$NbSi_2$.

The debinding treatment was chosen based on the curves shown in Figure 2 and on previous experience [5,88,89]. An isotherm at 70 °C for 10 h had the function of completing the evaporation of solvent, while a very slow heating rate, 0.25 °C/min, was used from 70 °C to 800 °C. The very slow heating had the function of avoiding the fast evolution of gases, which could cause the formation of bubbles, cracks and defects in the green ceramic. The maximum temperature was chosen as 800 °C, in order to provide an acceptable mechanical resistance to the specimens that will be transferred to the sintering oven.

Pressureless sintering was performed in a Pro.Ba. graphite furnace (Cambiano, Italy) at a temperature between 1600 and 1800 °C for 30 to 60 min. Based on these preliminary experiments, in this paper, we report only the results for the 1725–1785 °C range and 30 min sintering time, where the best results were obtained, and further characterisation was performed. The heating and cooling rates were 6 °C/min and the atmosphere was argon at a pressure of 600 mbar. During sintering, the samples were immersed in a mixture of powders of SiC (75 wt.%) and $NbSi_2$ (25 wt.%) inside graphite boxes.

The characterisation of the sintered samples included the analysis of the microstructure and of the crystalline phases, the measurement of density, mechanical properties and oxidation resistance. The geometric density of multilayers was measured in the green state, after debinding and sintering. In order to distinguish the open and closed porosity, apparent density of the sintered samples was also measured, using Archimede's method with water as a fluid. Picnometry was used to determine the theoretical density of $MoSi_2$ and $NbSi_2$. Young's modulus was measured on parallelepiped samples according to ASTM C 1259-21 [90] by using an impulse excitation technique, involving the analysis of the transient natural vibration (GrindoSonic MK5 Instrument, Leuven, Belgium), while Vickers microhardness (HV) was performed with a load of 500 g and a dwelling time of 10 s. Three-point bending strength was measured according to UNI EN 658.3 standard [91] (Sintech10D equipment, Shakopee, MN, USA), with a crosshead speed of 0.1 mm/min in stroke control and 40 mm span. For microscopy observation, rectangular samples were cut from the bending samples, mounted in transparent acrylic resin and polished down to 1 μm with diamond paste, and then cleaned in an ultrasonic bath with a mixture of water and ethanol, and subsequently etched to reveal the microstructure using a 20%vol HF, 40%vol HCl and 40%vol HNO_3 attack for 5 min, as reported by Nakano et al. [28]. The microstructure of the samples was assessed by scanning electron microscopy (SEM-FEG Assing SUPRA 25, Oberkochen, Germany), chemical composition by energy-dispersive spectroscopy (EDS Oxford, High Wycombe, United Kingdom), and phase composition by X-ray diffraction (Philips PW1710 $Cu_{K\alpha}$ radiation, Almelo, Netherlands). Thermogravimetric experiments were realised with a Mettler TG/SDTA 851e (Greifensee, Switzerland, performing runs in a controlled atmosphere (either air of argon) up to 1600 °C, at a rate of 10 °C/min.

3. Results and Discussion

3.1. Microstructure, Composition and Densification

In this work, $NbSi_2$ was used in a composition range between 5 and 20 wt.% of niobium disilicide, even if some samples were realised at high $NbSi_2$ content. The rationale behind this choice is that the structure with the most promising properties is the duplex one, where both $MoSi_2$ and $NbSi_2$ phases are present. Thermodynamic calculations demonstrate that the two silicides can be in pseudo-binary equilibrium [80], and this thermodynamic stability allows the formation of a duplex structure, due to the linkage of the crystallographic parameters of C11b ($MoSi_2$) and C40 ($NbSi_2$) structures, in the 5–20 wt.% $NbSi_2$ range [32]. For this reason, we investigated mainly the 5–20 wt.% of niobium disilicide, using pure $MoSi_2$ as a reference and higher $NbSi_2$ content samples to verify our assumption regarding the phases present after sintering.

In Figure 3, X-ray diffraction spectra of the inner portion of the samples fabricated at 1785 °C are presented, where the presence of the duplex structure is confirmed when $NbSi_2$ is added. The range 5–20 wt.% observed by Geng et al. [92] for the formation of duplex structures is confirmed by this analysis, while further increasing the niobium disilicide content up to 40 wt.% brings it to the single C40 phase, which is the same as with pure $NbSi_2$. The presence of other secondary phases, SiC, Mo_5Si_3, Nb_5Si_3, can be also observed, either present in the starting powders as impurities or formed in situ due to the reaction of the two disilicides with the carbon residua left by the organic components during the burning out.

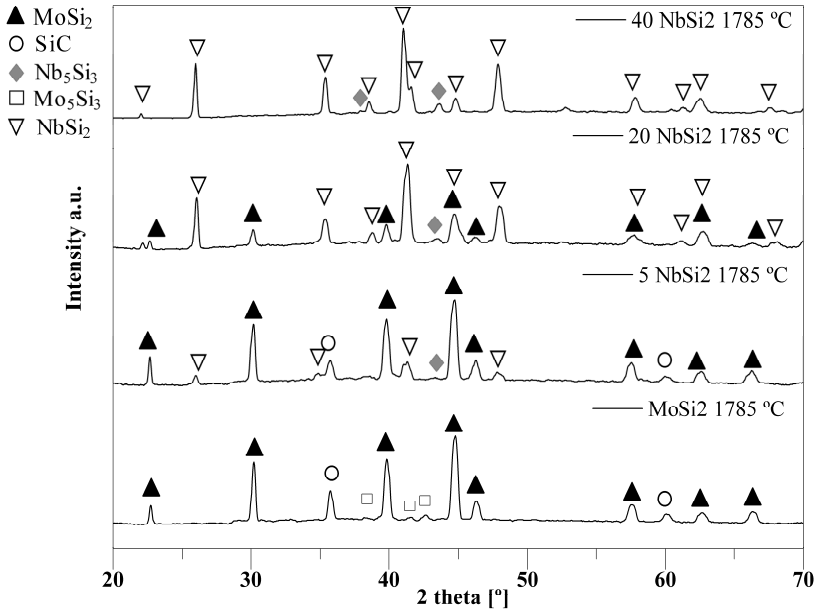


Figure 3. XRD spectra of $MoSi_2$–$NbSi_2$ multilayers sintered at 1785 °C: pure $MoSi_2$, 5 wt.% $NbSi_2$, 20 wt.% $NbSi_2$, 40 wt.% $NbSi_2$.

In the case of pure molybdenum disilicide, these secondary phases are SiC and Mo_5Si_3. A Rietveld refinement of the spectrum suggests around 35% of SiC and less than 5% of Mo_5Si_3 phase, which presents low peaks in the X-ray pattern but whose presence was confirmed by the EDS analysis. This phase probably derives from impurities in the powder (which is known to contain a small amount of the 5-3 silicide). Another possible source for the formation of Mo_5Si_3 is the reaction of $MoSi_2$ with carbon, which is widely study in the literature because the addition of carbon is one of the strategy routes to reduce or avoid the formation of the silica glassy phase generally observed in these compounds due to the high quantity of oxygen left around the particles of $MoSi_2$ and $NbSi_2$ during the powder-preparation step [3–7,93]. These SiO_2 inclusions were most often reported to be the cause of lower mechanical properties. In the presence of carbon, however, the literature suggests that not only is Mo_5Si_3 formed, but also Mo_5Si_3C, or $Mo_{4.8}Si_3C_{0.6}$, which belong to the class of Nowotny phases [5,93,94]. No such phase is observed in this case, so the origin of Mo_5Si_3 was ascribed only to impurities in the powders.

By increasing the niobium content, Mo_5Si_3 is no longer seen, while Nb_5Si_3 peaks are observed. Moreover, silicon carbide content decreases with niobium increase. A hint of NbC phase is observed in some cases, but the attribution is unclear. Rietveld refinement of the spectra suggests that in the sample containing 5 wt.% $NbSi_2$, the silicon carbide content decreases to under 30%, while a small quantity of $NbSi_2$ appears (around 10%). When increasing niobium disilicide to 20 wt.%, silicon carbide disappears, and the main phase becomes $NbSi_2$, at around 75%, with only traces of Nb_5Si_3, at around 1%, the rest being

$MoSi_2$. In the sample containing 40 wt.% $NbSi_2$, the $MoSi_2$ phase disappears, and only $NbSi_2$ (around 90%) and Nb_5Si_3 remain.

To better investigate the reason for the absence of Nowotny phase in the samples, XRD was also performed on the surface, where the carbon content is higher, probably due to the interaction with the oven atmosphere, and the results are shown in Figure 4, where the reported samples sintered at 1725 and 1750 °C.

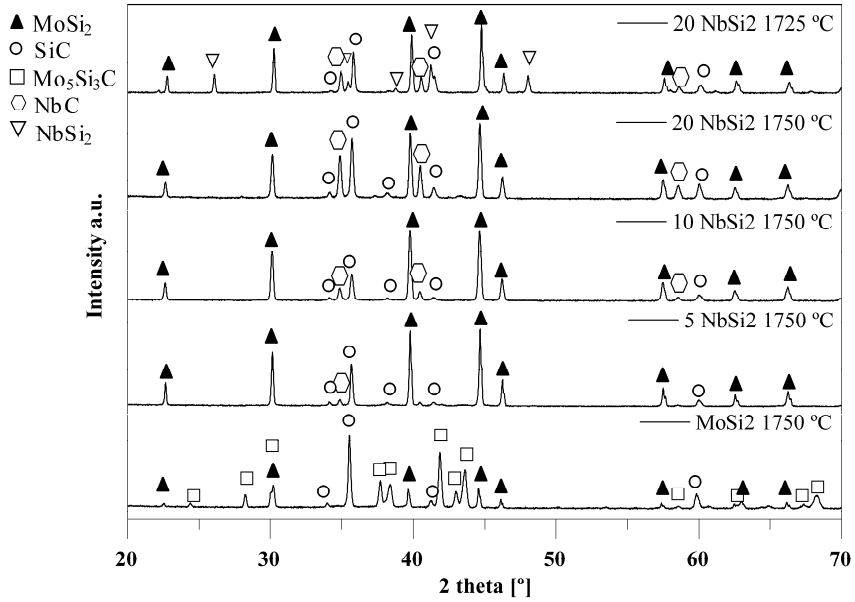


Figure 4. XRD pattern of the surface of $MoSi_2$-$NbSi_2$ multilayers, sintered at 1750 °C (pure $MoSi_2$, 5 wt.%$NbSi_2$, 10 wt.%$NbSi_2$, 20 wt.%$NbSi_2$) and at 1725 °C (20 wt.%$NbSi_2$).

In this case, the observed secondary phases are SiC, the Nowotny phase Mo_5Si_3C, and NbC. For pure $MoSi_2$, it is evident that with a higher carbon content, SiC and Mo_5Si_3C are formed. In particular, Rietveld refinement suggests less than 10% $MoSi_2$, around 50% of Nowotny phase and 45% of SiC.

With increasing $NbSi_2$ content, SiC quantity remains more or less constant, while NbC appears. Rietveld refinement suggests that NbC is present as 2–3% in the case of the sample containing 5% $NbSi_2$, increasing to around 5% in a 10% $NbSi_2$ sample, and to almost 15% in a 20% $NbSi_2$ one. In the literature, the most widely reported secondary products formed in the materials containing niobium disilicide are Nb_5Si_3C, and Nb_5Si_3. However, some evidence of NbC formation is seen, for instance, by Yaney et al. [95], who observed the formation of NbC as a primary reaction product when they studied Nb–Si–C–O reaction systems. In their investigation, it was reported that high quantities of oxygen and carbon in the reaction seems to promote the formation of NbC. In the ternary phase diagram of the Nb–Si–C system, they reported that while $NbSi_2$ and SiC can be in equilibrium, the presence of the Nb_5Si_3 phase promotes the formation of NbC. Thus, the presence of Nb_5Si_3 in this system can also promote the formation of niobium carbide.

Moreover, on the surface, no C40 ($NbSi_2$) phase is observed even in the case of niobium-rich compositions, for the samples sintered at 1750 and 1785 °C. At 1725 °C, only with 20 wt.%$NbSi_2$ the C40 phase is observed (between 15 and 20%), while at lower Nb concentration there is only the $C11_b$ phase ($MoSi_2$). These results suggest that a higher carbon content pushes the reaction toward the Nowotny phase in the case of pure $MoSi_2$, and toward NbC in the case of $NbSi_2$-containing samples, consuming the niobium and leaving the $C11_b$ phase as the predominant one. Instead, at low carbon content, i.e., in the interior of the samples, only a small amount of SiC is formed, and the two silicides

are rather stable, with the coexistence of the C40 and $C11_b$ phases. Another important observation is that with Nb substitution, no Nowotny phase is observed. This confirms that niobium suppresses the formation of Mo_5Si_3C phase, promoting instead the formation of NbC.

The microstructure of the materials sintered at the three different temperatures (1725, 1750 and 1785 °C) is reported in Figures 5, 6 and 7, respectively. Case (A) represents pure $MoSi_2$, case (B) 5%$NbSi_2$, case (C) 10%$NbSi_2$, and case (D) 20%$NbSi_2$. These images are taken with backscattered electrons, so the different phases exhibit different shades of grey. $MoSi_2$ is the medium grey phase, SiC the dark phase (since it has the lowest mean atomic number) and Mo_5Si_3 or Nb_5Si_3 are the brighter phase (since they have the highest mean atomic number). In these images, it is not possible to distinguish between molybdenum and niobium, since their atomic number is very similar. Umakoshi, Nakano and co-workers in their investigations were able to see a difference between the two silicides in SEM images only when they annealed the samples to obtain a lamellar structure, and only with compositions with 10 and 15 wt.% of $NbSi_2$ [24–32]. In this case, EDS was used instead to measure the relative Mo and Nb content. It must also be mentioned that at 1725 °C, the different phases are not very easily distinguished, due to the smaller grain size and to the high residual porosity content evidenced in Figure 5. In particular, the Mo_5Si_3 or Nb_5Si_3 phase begins to be clearly observed only at 1750 °C.

At 1725 °C, for pure $MoSi_2$, the SiC grains are mostly extremely small, in the submicrometric range, and are well-distributed in the matrix material, helping to control the growth of $MoSi_2$ grains. As already anticipated in the discussion of XRD results, the main reason of the formation of this phase is the reaction of carbon from the organic component of the slip with silicon oxide or molybdenum disilicide, following these reactions:

$$SiO_2 + 3\,C \rightarrow SiC + 2\,CO \quad (3)$$

$$5\,MoSi_2 + 7\,C \rightarrow Mo_5Si_3 + 7\,SiC \quad (4)$$

$$5\,MoSi_2 + 8\,C \rightarrow Mo_5Si_3C + 7\,SiC \quad (5)$$

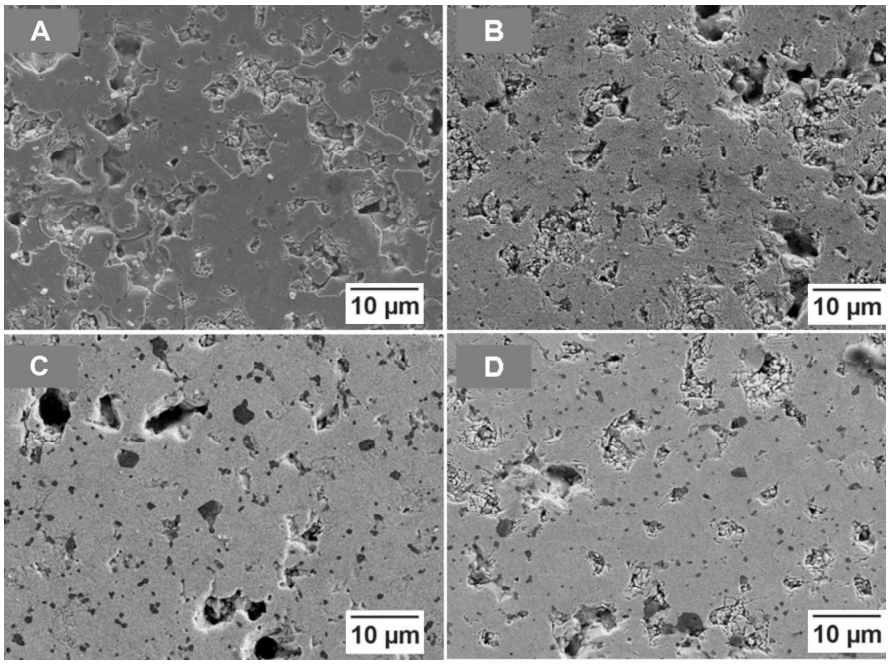


Figure 5. Backscattered electrons SEM images of multilayers sintered at 1725 °C for 30 min: (**A**) $MoSi_2$; (**B**) 95%$MoSi_2$–5%$NbSi_2$; (**C**) 90%$MoSi_2$–10%$NbSi_2$; (**D**) 80%$MoSi_2$–20%$NbSi_2$.

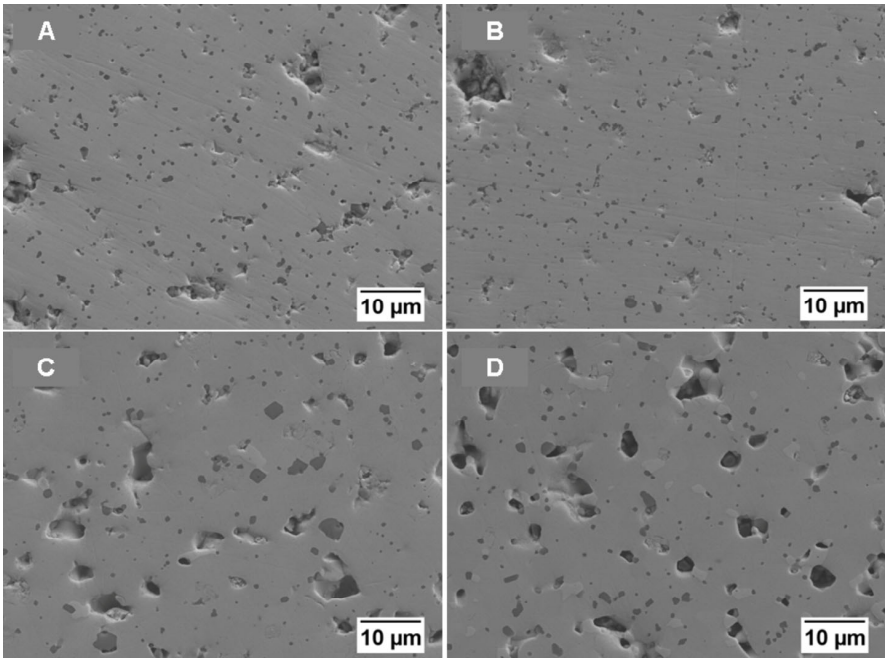


Figure 6. Backscattered electrons SEM images of multilayers sintered at 1750 °C for 30 min: (**A**) $MoSi_2$; (**B**) 95%$MoSi_2$–5%$NbSi_2$; (**C**) 90%$MoSi_2$–10%$NbSi_2$; (**D**) 80%$MoSi_2$–20%$NbSi_2$.

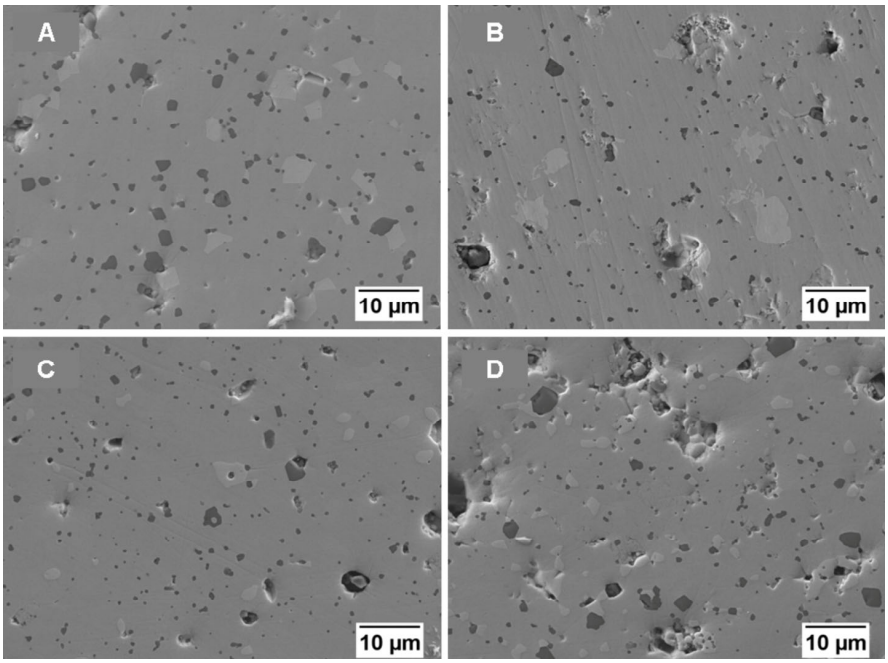


Figure 7. Backscattered electrons SEM images of multilayers sintered at 1785 °C for 30 min: (**A**) $MoSi_2$; (**B**) 95%$MoSi_2$–5%$NbSi_2$; (**C**) 90%$MoSi_2$–10%$NbSi_2$; (**D**) 80%$MoSi_2$–20%$NbSi_2$.

The SiO_2 into the $MoSi_2$ matrix in some reports is located at the grain boundaries, wetting the $MoSi_2$ grains, and in others, within the grains; other works found the silica inclusions in both locations [3–7,93]. The in situ formation of SiC seems to have the same behaviour, irrespective of where the SiO_2 is positioned. If the silica is in the grain boundary, the SiC will be there, and the same will happen when it is located inside the grain. Thus, the silicon carbide grains appear well-distributed among the $MoSi_2$ ones. The predominant mechanism of SiC formation is probably given by reaction (3), since no Nowotny phase is observed by XRD and the Mo_5Si_3 phase is already present in the powders. It is not

possible to exclude the contribution of reaction (4), while, contrary to what is suggested in the literature, reaction (5) was not observed.

For samples containing $NbSi_2$, it is possible to note how SiC grains increase in size with respect to the pure $MoSi_2$ case, reaching the micron range for 10 wt.% and 20 wt.%$NbSi_2$-containing samples.

Increasing the temperature (to 1750 °C and 1785 °C, Figures 6 and 7, respectively) allows for grain growth, and the secondary phases (SiC, Mo_5Si_3 or Nb_5Si_3, and NbC in the case of high niobium content) become more evident. In Table 2, the image analysis results, in terms of area-weighted distribution of SiC particle diameter, are reported for the samples sintered at 1750 and 1785 °C. The correspondence with the SEM images is clear, suggesting that the smaller SiC grain size is observed for the samples containing 5%$NbSi_2$.

Table 2. Image analysis results on SiC phase for the $MoSi_2$/$NbSi_2$ materials sintered at 1750 and 1785 °C: grain size distribution parameters.

Sintering *T*	**1750 °C**				**1785 °C**			
Sample	**$MoSi_2$**	**5%$NbSi_2$**	**10%$NbSi_2$**	**20%$NbSi_2$**	**$MoSi_2$**	**5%$NbSi_2$**	**10%$NbSi_2$**	**20%$NbSi_2$**
d10	0.45	0.4	0.52	0.55	0.7.	0.4	0.45	0.55
d50	0.9	0.75	1.5	1.2	1.5	0.85	0.95	1.4
d90	1.6	1.2	3.4	2.2	3.3	1.5	2.5	3.8

In detail, at 1750 °C, both in the pure $MoSi_2$ and in the 5 wt.% $NbSi_2$ samples it is still observed a large fraction of the submicrometric SiC phase (d50 is smaller than 1 μm). Instead at 10 wt.% and 20 wt.% $NbSi_2$ a larger amount of micrometric SiC grains is observed, with also a slight formation of NbC, as also confirmed by EDS analysis. The 5-3 silicide grains are typically larger than the SiC ones, generally over 1 μm, but at 1750 °C, they are observed only with 10% or 20%$NbSi_2$.

At the highest temperature used, 1785 °C, the microstructure presents a larger grain size both for the secondary phases and for the silicides. In all compositions, the presence of Mo_5Si_3 or Nb_5Si_3 silicides was observed even when not clearly observed by XRD analysis. Again, the size of 5-3 silicides was over 1 μm, while no significant differences in the grain size distributions were observed as a function of niobium silicide content. The SiC grains remain instead rather small, even if they are larger than at 1750 °C in the pure $MoSi_2$ case.

As already anticipated, a very interesting behaviour of all the samples, both of pure molybdenum disilicide and containing niobium, was that no silica glassy phase was ever observed after sintering. The reason for this very positive effect must probably be searched in the use of tape casting as the processing method; the silica reduction process probably starts during the debinding phase, and ends during the sintering thanks to the small carbonaceous residua left from the decomposition of binder, plasticiser and other organic components of the slurry. Thus, there is no need to add carbon directly to the powders, as it is performed with other techniques, like hot pressing. As described in the discussion of Figure 4, avoiding the addition of an excessive quantity of carbon should also be beneficial in terms of phase formation, since lower amounts of brittle Nowotny phase, SiC and NbC are formed.

The open and total porosity data for the $MoSi_2$–$NbSi_2$ multilayers are shown in Figure 8, where filled markers represent total porosity and unfilled markers represent open porosity. Total porosity data demonstrate that an increase in temperature causes a better densification of the materials, as confirmed by the microstructures (Figures 5–7), where a reduction in the porosity is observed at a higher temperature, even if the pores can grow

due to the coalescence of the small ones. A smaller and more uniform pore distribution, even if the number of pores is greater, is present in the samples sintered at 1725 °C.

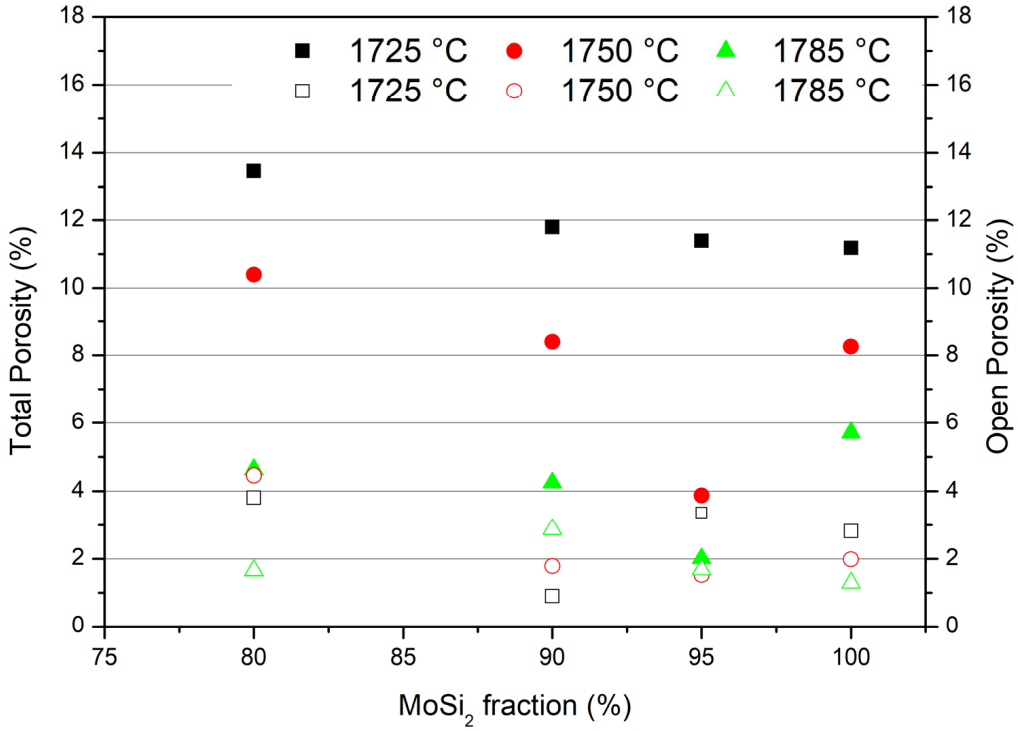


Figure 8. Total porosity (filled markers) and open porosity (unfilled markers) of $MoSi_2$–$NbSi_2$ sintered multilayers at 1725 °C (■,□) 1750 °C (●,○) and 1785 °C (▲,△).

Similar results were obtained by Biamino et al. [5] on multilayers of pure $MoSi_2$, where the relative density of samples sintered at 1700 °C and 1750 °C were around 85 and 88%, respectively. It must be also considered that the samples of pure $MoSi_2$ of the Biamino paper were sintered using carbon as protective powder, while in this case, the samples were immersed in a mixture of powders of SiC and $NbSi_2$ inside graphite boxes in order to limit the possible reaction of niobium disilicide with carbon. By limiting the reaction with carbon, an increase in the final density was observed. Some tests performed with a higher sintering time (60 min) suggested that the increase in sintering time did not provide further benefit in densification.

Regarding the effect of niobium silicide introduction, the addition of a small quantity of $NbSi_2$ (5%) caused an enhancement in densification in the multilayers, at 1750 and 1785 °C; with respect to pure $MoSi_2$, the total porosity is only 4% and 2%, respectively. When the fraction of $NbSi_2$ increases further, the density goes down again, and densification values similar to the pure molybdenum disilicide are found. At 1725 °C, the increase in niobium silicide content causes a small reduction in the density.

Open porosity is also reported in Figure 8 because it is important for oxidation behaviour (see Section 3.3). The trend is unclear; however, open porosity is generally higher for the samples with low overall density and for those sintered at higher temperature.

3.2. Mechanical Properties

The trend observed for density is generally clearly reflected in the elastic modulus, for all the studied compositions. In Figure 9, data for relative density (diamond symbol), Young's modulus (triangle symbol) and modulus of rupture (square symbol) are plotted against the $MoSi_2$ fraction for the three sintering temperatures. There are no significant differences between the trend of the values of the Young's modulus and

the one of the density, with the lowest values observed for high $NbSi_2$-containing samples and low sintering temperature. If the sintering temperature increases, as already observed in the density case, the Young's modulus increases up to close to 400 GPa. This behaviour is shown more clearly in Figure 10, where the correlation between Young's modulus and density is presented as a function of sintering temperature for the different studied compositions.

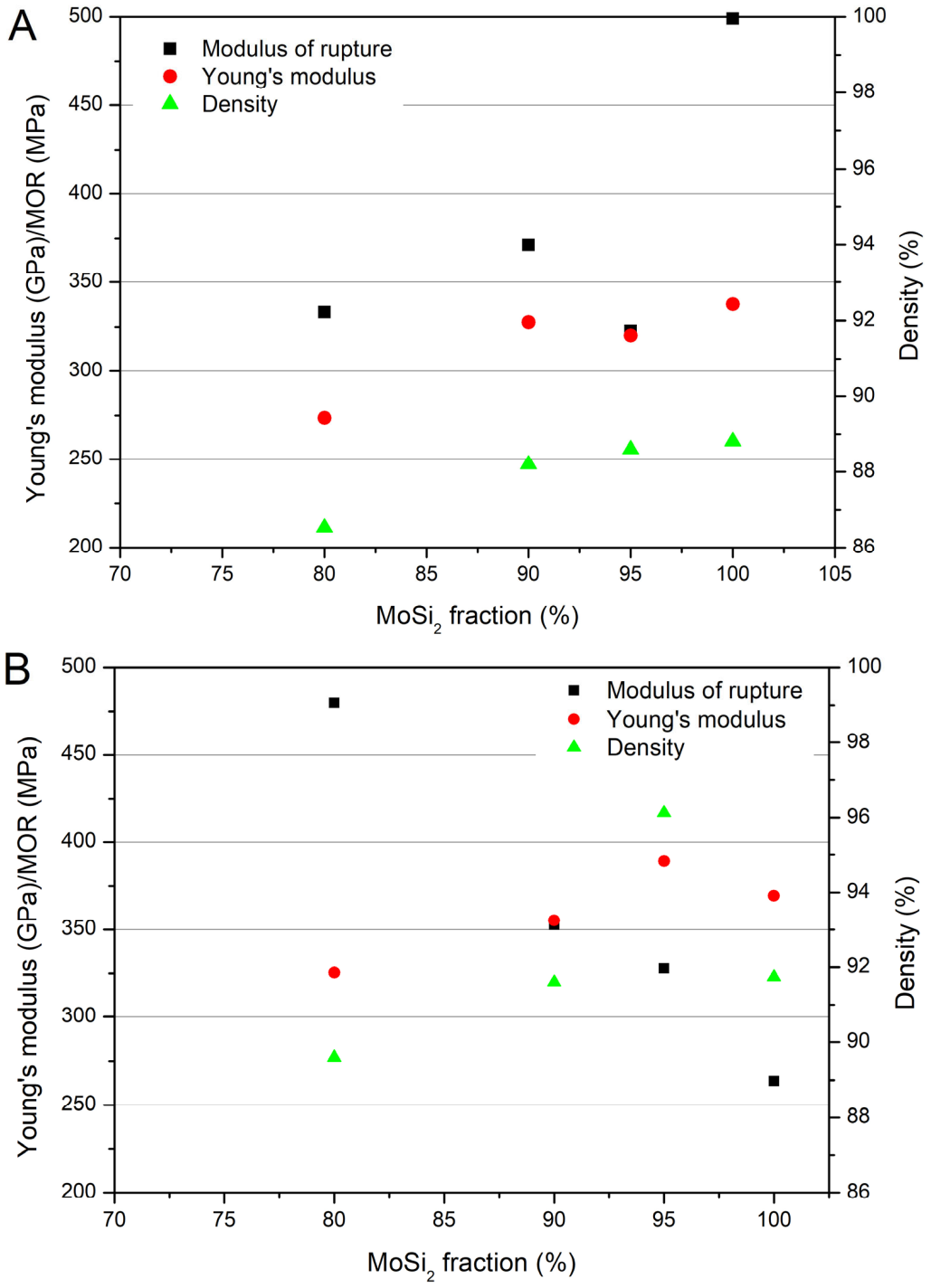


Figure 9. *Cont.*

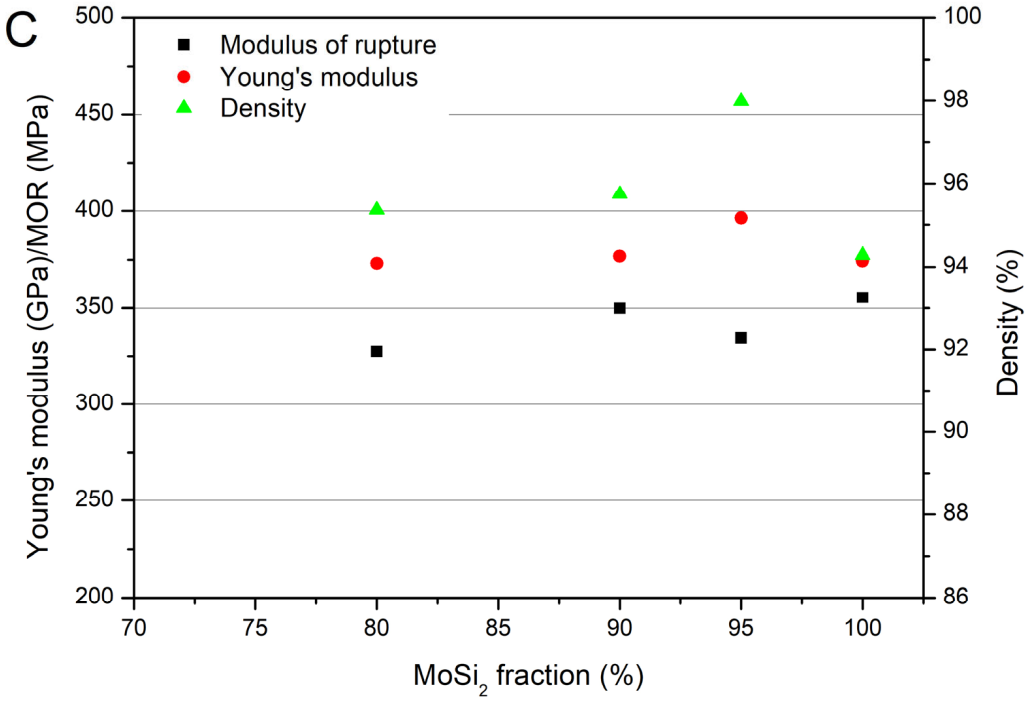


Figure 9. Relative density (▲, right-hand *y* axis), Young's modulus (●, left-hand *y* axis) and modulus of rupture (MOR) (■, left-hand *y* axis) of the multilayers sintered at (**A**) 1725, (**B**) 1750 and (**C**) 1785 °C as a function of $MoSi_2$ content.

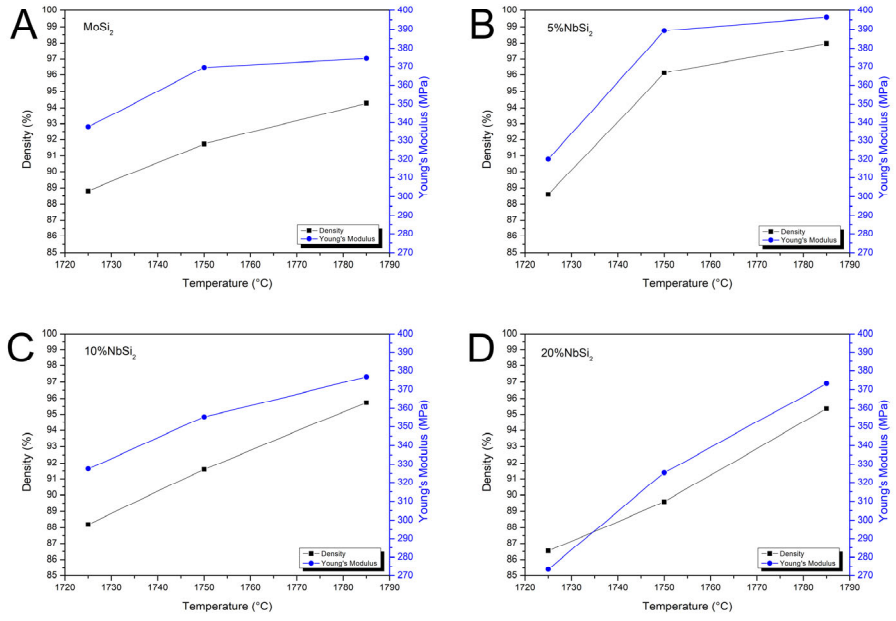


Figure 10. Relationship between relative density (■) and Young's modulus (●) as a function of temperature for the different compositions: (**A**) $MoSi_2$, (**B**) 5%$NbSi_2$, (**C**) 10%$NbSi_2$, and (**D**) 20%$NbSi_2$.

At a sintering temperature of 1725 °C, the minimum addition of 5 wt.% $NbSi_2$ (Figure 10B) had a negligible effect on the density but reduced the Young's modulus compared to the pure $MoSi_2$ (Figure 10A). However, at higher sintering temperatures, the most substantial increase in both density and Young's modulus was observed. A further increase in the $NbSi_2$ content (10 wt.% and 20 wt.%) leads to a more pronounced decrease in the material's density, particularly at low (1725 °C) and medium (1750 °C) temperatures, compared to pure $MoSi_2$ (Figure 10C,D). Conversely, at the highest sintering temperature

of 1785 °C, all samples with 10 wt.% $NbSi_2$ and 20 wt.% $NbSi_2$ exhibited a marginally improved density and a comparable Young's modulus.

Regarding the modulus of rupture/bending strength, a complex behaviour is observed. It is interesting to observe both the strength versus sintering temperature and the strength versus $NbSi_2$ fraction trends.

In the first case, with pure $MoSi_2$, the small size of pores and grains observed for the samples sintered at 1725 °C allows for higher bending strength (up to almost 500 MPa), while at higher temperatures, the mechanical resistance is reduced due to the increase in the size of both pores and secondary brittle phases. This behaviour is similar to the one observed in [5], where the increase in density and Young's modulus was accompanied by a decrease in bending strength. The decrease is not linear with temperature probably because two phenomena are occurring at the same time: reduction in strength due to the increase in pore and grain size, and increase in strength due to the increase in density. At a sintering temperature of 1725 °C, the addition of $NbSi_2$ causes a reduction in bending strength with respect to pure $MoSi_2$, with values ranging between 320 and 370 MPa. This reduction can be partially related to the density, but also to the increase in the size of the silicon carbide precipitates, as observed in Figures 5–7. Also the phase composition could play a role, with the opposite behaviour of the brittle NbC phase, reducing strength, and of the duplex structure, which can increase the mechanical properties of $MoSi_2$–$NbSi_2$ materials [25,27,29,31,32,96].

The samples sintered at 1750 °C present a different behaviour with respect to those sintered at 1725 °C. It is evident from Figure 9 that the addition of $NbSi_2$ has a positive effect in this case, and the samples containing 20 wt.% of $NbSi_2$ present a very high strength, 480 MPa. To explain this phenomenon, two causes can be considered. The first concerns the crack deflection mechanism at the interfaces between different layers. The tapes containing high amounts of niobium silicide, in particular the 20 wt.% $NbSi_2$ one, present a higher surface roughness with respect to the pure $MoSi_2$ ones, probably due to the presence of the fraction of the larger-sized $NbSi_2$ powder in the slurry. The tapes are superimposed so that a rough surface adheres to a smooth one (the one in contact with the Mylar sheet); the rougher the tape, the higher the porosity level at the interface between each of the layers of the multilayer. In Figure 11, it is possible to observe the fracture surface of 20 wt.% $NbSi_2$ sample (Figure 11B) compared with a pure $MoSi_2$ one (Figure 11A). The samples are well-sintered, save for the interlayer zone marked with black arrows in Figure 11B, where long interconnected pores are present. These porous zones can promote crack deflection, as happens in layered structures with porous interlayers or weak interfaces [32,97]. In Figure 11C,D, a magnification of the porous zone evidenced by the black arrows is presented, in order to better show the porous zone that facilitates crack deflection. The other possible cause of the increase in the strength of samples sintered at 1750 °C with niobium silicide content is related to the presence of the duplex structure, where the C11b phase act as a minority reinforcement for the C40 phase, as shown by XRD data and confirmed by the literature [31,32,96]. This type of structure was suggested to be effective in strengthening the material [25,27,29], since the C11b phase was shown to prevent the initial rapid propagation of cracks, causing crack deflection and improving ductility.

The microhardness behaviour is also shown in Figure 12. The hardness increases with the sintering temperature, i.e., with the density, and decreases in the presence of $NbSi_2$. The presence of niobium silicide negatively affects the hardness, probably due to the presence of the brittle NbC phase.

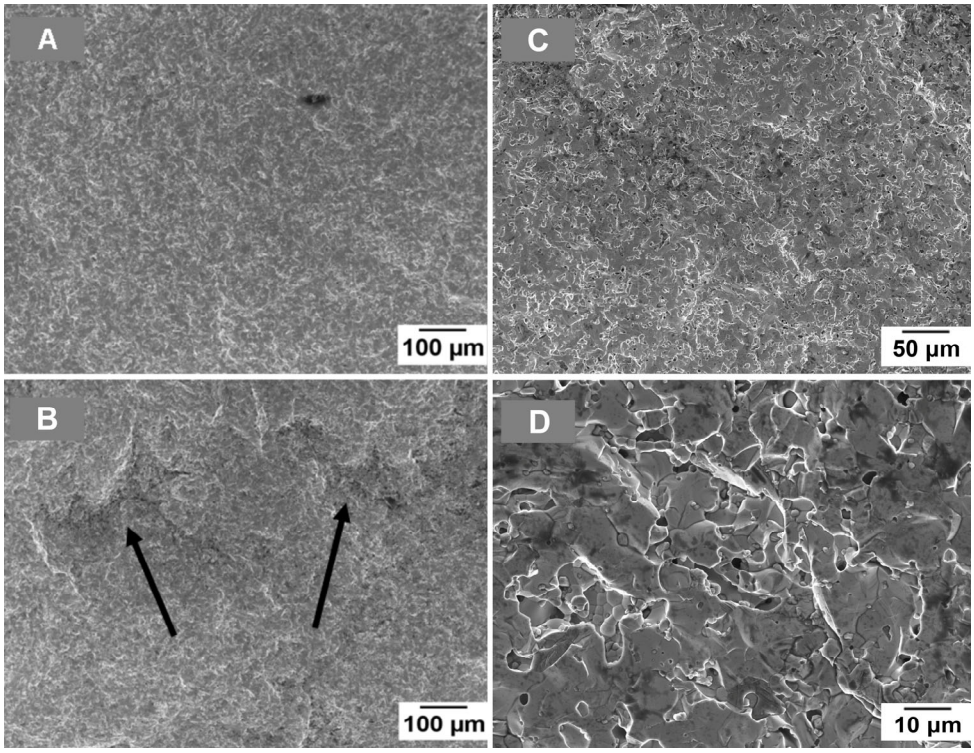


Figure 11. Fracture surface of samples sintered at 1750 °C: (**A**) pure $MoSi_2$, (**B**) $MoSi_2$–20%$NbSi_2$, (**C**,**D**) higher magnification images of the interlayer zone; black arrows in (**B**) indicate the interface between different layers.

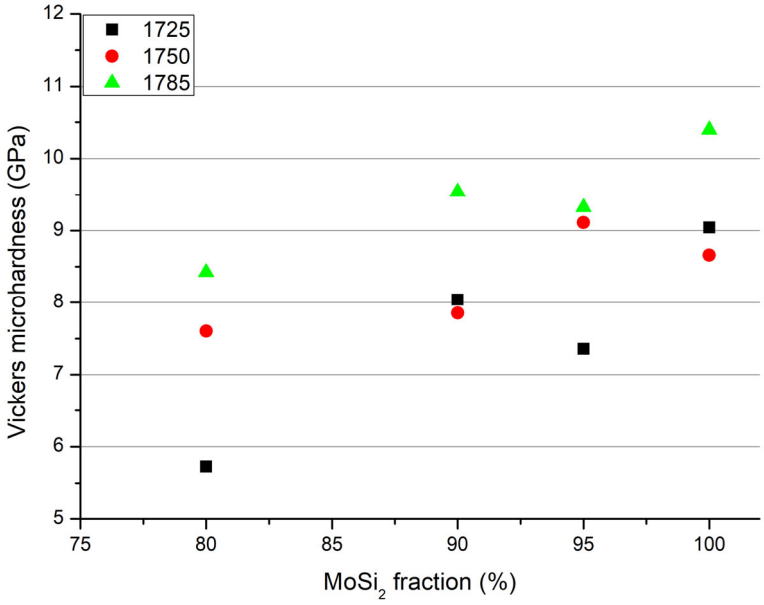


Figure 12. Vickers microhardness of samples sintered at 1725 °C, 1750 °C and 1785 °C, as a function of $NbSi_2$ content.

3.3. Oxidation Behaviour

As already mentioned in the introduction, $MoSi_2$ has a great potential as a structural material for application at high temperature due to its outstanding oxidation resistance at high temperature, but the issues connected with the pest oxidation must be overcome [11–15]. In this study, the oxidation behaviour of the $MoSi_2$–$NbSi_2$ materials was realised through thermogravimetric experiments. In Figure 13, TGA curves of the multilayers of all the compositions are reported for samples sintered at 1725, 1750 and 1785 °C.

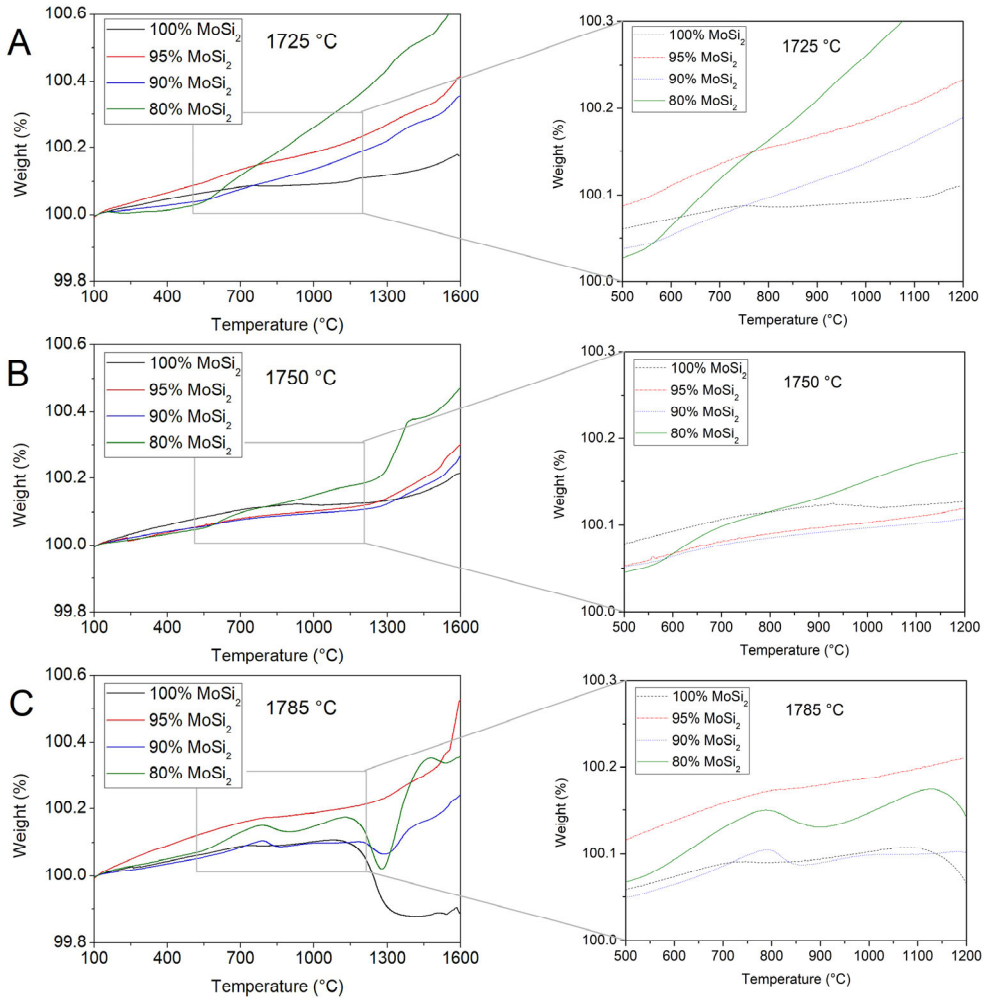


Figure 13. TGA curves of samples sintered at 1725 °C (**A**), 1750 °C (**B**) and 1785 °C (**C**), for samples with different $MoSi_2$ content. On the right side, a magnification of the zone between 500 and 1200 °C, the pest oxidation region, is presented.

In general, when analysing oxidation curves, three important characteristics of the material must be kept into account: first, the composition, which is the main driver to the oxidation resistance; second, the open porosity of the samples, which determines the amount of surface accessible to the oxidising atmosphere, and thus the overall weight gain; third, the grain size, which will determine the homogeneity of the oxidised layer: if the grains are small, the layer will have more uniform composition and less residual stresses at the interfaces. If the grains are large, spalling of the oxidised layer will be easier.

The curves of samples obtained at 1725 and 1750 °C are rather similar (Figure 13A and 13B, respectively). The pure $MoSi_2$ samples (black curves) show a limited weight increase at high temperature, demonstrating a good passivation behaviour, but present a plateau in the curve between 700–800 °C and 1100–1200 °C. The plateau is due to the balance between $MoSi_2$ oxidation and MoO_3 evaporation, and its presence confirms pest oxidation behaviour [12–14,75,98]. With the addition of small quantities of niobium disilicide, the plateau is not observed anymore, and the weight grows steadily with the temperature. This suggests that a change in the oxidation mechanism occurs, as observed also by several authors for boron addition [12,75,76]. Too high a $NbSi_2$ quantity, however, is not beneficial to the oxidation resistance, for two reasons. First, Nb_2O_5 can be formed upon oxidation [99–103], which can have several effects. It can reduce the compactness of the oxide layer, thus causing higher oxidation rates. Additionally, it is known to cause

spallation of the oxidised coating due to significant volume changes [103]. Finally, it can form elongated grains [100,102] that reduce the cohesion of the layer. Second, NbC is also present, and it can generate internal cracks when the ratio of the $NbSi_2$–Nb_5Si_3–NbC–SiC is not appropriated [95], since it can act as nucleation site for the oxidation mechanism.

The samples sintered at 1785 °C (Figure 13C) present complex curves that could be interpreted as taking into account the bigger mean grain size, and thus less homogeneity of the layer, and the higher open porosity (as shown in Figure 9, except for the 20 wt.% $NbSi_2$ samples). In particular, spalling phenomena can cause a sudden weight increase, while evaporation causes a plateau of or a gradual decrease in weight in the curve. Also at this temperature, the best sample is the one containing 5 wt.% $NbSi_2$, which does not present evident MoO_3 evaporation or spalling phenomena.

The morphology after oxidation of the sample with 5 wt.% $NbSi_2$ sintered at 1750 °C, which has the best oxidation behaviour, is depicted in Figure 14. SEM observation demonstrated the presence of two layers close to the surface: the underlying $MoSi_2$ is indicated with the number 3; a region is then observed (number 2) containing SiO_2 and molybdenum silicides (both $MoSi_2$ and Mo_5Si_3); and finally, a dense layer of pure silica (number 1) that avoids the further oxidation of the sample.

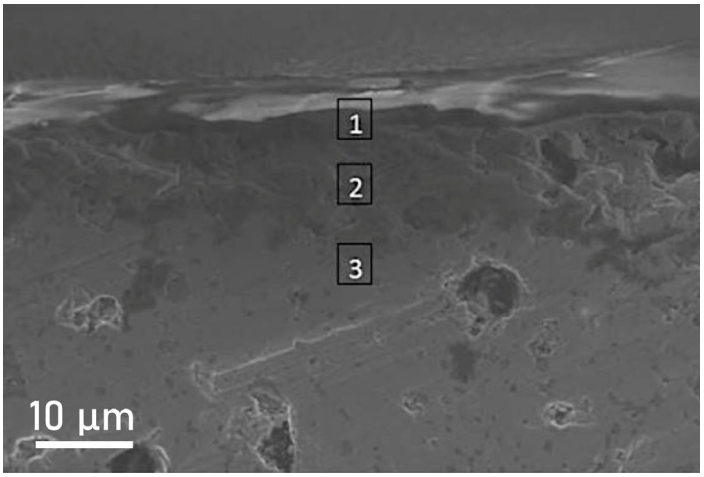


Figure 14. SEM image of the sample with 5 wt.% $NbSi_2$ sintered at 1750 °C.

From all these data, it is possible to try to draw some conclusions. First, it seems evident that the sintering temperature must be strictly controlled to guarantee, at the same time, a proper densification and limited secondary reactions. If, at 1785 °C, the density, Young's modulus and microhardness are higher, it is clear that oxidation resistance decreases. The formation of larger grains probably reduces the ability of the material to properly withstand oxidation without spalling of the oxide layer.

Regarding the optimal amount of $NbSi_2$, the data suggest that 5% or 10% are the best cases. From a mechanical point of view, pure $MoSi_2$ or 20%$NbSi_2$ can give very good results, but pest oxidation is present in the case of pure $MoSi_2$, while a too-high oxidation rate is observed when 20% $NbSi_2$ is used, probably due to the formation of a layer with reduced protective ability.

The reason for this behaviour can be inferred by crossing the information of XRD and microstructural observations. Diffraction spectra show that a duplex microstructure is obtained when a small quantity of $NbSi_2$ is added; moreover, using only 5% of $NbSi_2$ allows a better densification at both 1750 and 1785 °C, with higher density and Young's modulus, and a limited grain growth. The samples with 10% $NbSi_2$ have higher porosity and grain size but comparable mechanical properties. The density and microstructure observed for the samples sintered at 1750 °C allows for the best oxidation resistance, which

requires an absence of pest oxidation, as also observed by Huang and coworkers with WSi_2 [79]. These authors discuss in detail the effect of WSi_2 on the oxidation resistance of $MoSi_2$–20%Al_2O_3 composites, concluding that it is due to two factors: the limited diffusion of Si atoms when W is present, and the consequent limited thickness of the oxide layer, which limit the rupture and peeling of the oxide layer. It must be stressed, however, that these authors use a $MoSi_2$–20%Al_2O_3 composite, and that their oxide layer also contains Al_2O_3 in a mullite form. In this case, the presence of a duplex structure could work in a similar way, hindering the diffusion of silicon, but the presence of $NbSi_2$ probably also has the effect of limiting MoO_3 formation. A similar effect was observed by Li et al. [104], who added chromium to $MoSi_2$ to obtain a duplex structure between C40 and C11b, as in this case, claiming an increase in oxidation resistance.

In conclusion, it seems that the best samples are those containing 5 wt.% or 10 wt.% $NbSi_2$, sintered at 1750 °C, where the best coupling of mechanical properties (modulus or rupture and Young's modulus) and oxidation resistance is obtained.

4. Conclusions

In this work, molybdenum disilicide multilayers were prepared by the tape-casting technology followed by pressureless sintering, studying the effect of the addition of a small fraction of $NbSi_2$ on densification, microstructure, mechanical properties and oxidation resistance. The results show that a small amount (5 wt.%) of niobium silicide can improve the density, Young's modulus and oxidation resistance of $MoSi_2$, even if the flexural strength is reduced. The sintering temperature had a significant effect on the properties, and it was shown that it is important to find an equilibrium between lower sintering temperature, which results in higher porosity but smaller pores and less intensive reactions between the components, and higher sintering temperature, which reduces the porosity but results in an increase in the pore size and in the open porosity, thus causing higher stiffness but lower strength and lower oxidation resistance. The best compromise between strength, stiffness and oxidation resistance was found for 5 wt.% $NbSi_2$ at 1750 °C sintering temperature, where good values for stiffness (350 GPa) and flexural strength (>300 MPa) were obtained, together with the best oxidation resistance and no evident pest oxidation. Moreover, the silica glass inclusions that form during sintering are reduced during the processing route thanks to the products of the decomposition of the organic components of the slurry necessary for the tape casting.

Author Contributions: Conceptualisation, C.B. and M.P.; methodology, C.B., S.B. and M.P.; software, L.L.; validation, D.M.V., E.P. and S.B.; formal analysis, D.M.V. and E.P.; investigation, D.M.V. and E.P.; resources, C.B.; data curation, M.P. and L.L.; writing—original draft preparation, D.M.V.; writing—review and editing, D.M.V., E.P., C.B., S.B., L.L. and M.P.; visualisation, D.M.V., L.L. and M.P.; supervision, C.B. and M.P.; funding acquisition, D.M.V., M.P. and S.B. All authors have read and agreed to the published version of the manuscript.

Funding: This research received no external funding.

Data Availability Statement: The original contributions presented in this study are included in the article. Further inquiries can be directed to the corresponding author.

Conflicts of Interest: The authors declare no conflicts of interest.

References

1. Jiang, L.; Zheng, B.; Wu, C.; Li, P.; Xue, T.; Wu, J.; Han, F.; Chen, Y. A Review of Mo-Si Intermetallic Compounds as Ultrahigh-Temperature Materials. *Processes* **2022**, *10*, 1772. [CrossRef]
2. Tapia-López, J.; Pech-Canul, M.I.; García, H.M. Processing, Microstructure, Properties, and Applications of $MoSi_2$-Containing Composites: A Review. *Front. Mater.* **2023**, *10*, 1165245. [CrossRef]

3. Petrovic, J.J.; Vasudevan, A.K. Key Developments in High Temperature Structural Silicides. *Mater. Sci. Eng. A* **1999**, *261*, 1–5. [CrossRef]
4. Petrovic, J.J. Toughening Strategies for $MoSi_2$-Based High Temperature Structural Silicides. *Intermetallics* **2000**, *8*, 1175–1182. [CrossRef]
5. Biamino, S.; Antonini, A.; Pavese, M.; Fino, P.; Badini, C. $MoSi_2$ Laminate Processed by Tape Casting: Microstructure and Mechanical Properties' Investigation. *Intermetallics* **2008**, *16*, 758–768. [CrossRef]
6. Vasudévan, A.K.; Petrovic, J.J. A Comparative Overview of Molybdenum Disilicide Composites. *Mater. Sci. Eng. A* **1992**, *155*, 1–17. [CrossRef]
7. Bewlay, B.P.; Jackson, M.R.; Subramanian, P.R.; Zhao, J.-C. A Review of Very-High-Temperature Nb-Silicide-Based Composites. *Metall. Mater. Trans. A* **2003**, *34*, 2043–2052. [CrossRef]
8. Yao, Z.; Stiglich, J.; Sudarshan, T.S. Molybdenum Silicide Based Materials and Their Properties. *J. Mater. Eng. Perform.* **1999**, *8*, 291–304. [CrossRef]
9. Cabouro, G.; Chevalier, S.; Gaffet, E.; Grin, Y.; Bernard, F. Reactive Sintering of Molybdenum Disilicide by Spark Plasma Sintering from Mechanically Activated Powder Mixtures: Processing Parameters and Properties. *J. Alloys Compd.* **2008**, *465*, 344–355. [CrossRef]
10. Sharif, A.A.; Misra, A.; Petrovic, J.J.; Mitchell, T.E. Solid Solution Hardening and Softening in $MoSi_2$ Alloys. *Scr. Mater.* **2001**, *44*, 879–884. [CrossRef]
11. Chirkin, A.D.; Lavrenko, V.O.; Talash, V.M. High-Temperature and Electrochemical Oxidation of Transition Metal Silicides. *Powder Metall. Met. Ceram.* **2009**, *48*, 330–345. [CrossRef]
12. Potanin, A.Y.; Pogozhev, Y.S.; Levashov, E.A.; Novikov, A.V.; Shvindina, N.V.; Sviridova, T.A. Kinetics and Oxidation Mechanism of $MoSi_2$–MoB Ceramics in the 600–1200 °C Temperature Range. *Ceram. Int.* **2017**, *43*, 10478–10486. [CrossRef]
13. Samadzadeh, M.; Oprea, C.; Karimi Sharif, H.; Troczynski, T. Comparative Studies of the Oxidation of $MoSi_2$ Based Materials: Low-Temperature Oxidation (300–900 °C). *Int. J. Refract. Met. Hard Mater.* **2017**, *66*, 11–20. [CrossRef]
14. Samadzadeh, M.; Oprea, C.; Karimi Sharif, H.; Troczynski, T. Comparative Studies of the Oxidation of $MoSi_2$ Based Materials: High-Temperature Oxidation (1000–1600 °C). *Int. J. Refract. Met. Hard Mater.* **2017**, *69*, 31–39. [CrossRef]
15. Magnani, G.; Brentari, A.; Burresi, E.; Coglitore, A. Mechanical Properties and Oxidation Behavior of Silicon Carbide–Molybdenum Silicides Composites. *Ceram. Int.* **2013**, *39*, 3345–3351. [CrossRef]
16. Tao, X.; Xu, X.; Xu, X.; Hong, W.; Guo, A.; Hou, F.; Liu, J. Self-Healing Behavior in $MoSi_2$/Borosilicate Glass Composite. *J. Eur. Ceram. Soc.* **2017**, *37*, 871–875. [CrossRef]
17. Friák, M.; Holec, D.; Šob, M. Quantum-Mechanical Study of Nanocomposites with Low and Ultra-Low Interface Energies. *Nanomaterials* **2018**, *8*, 1057. [CrossRef] [PubMed]
18. Betsofen, S.Y.; Lozovan, A.A.; Lenkovets, A.S.; Sokolov, I.V. Study of the Phase Composition of Silicide Coatings, Based on Layered Nb-Mo Structures, Obtained by Vacuum-Arc Deposition. *J. Surf. Investig. X-Ray Synchrotron Neutron Tech.* **2015**, *9*, 225–230. [CrossRef]
19. Yuge, K.; Koizumi, Y.; Hagihara, K.; Nakano, T.; Kishida, K.; Inui, H. First-Principles Study on Phase Stability of $MoSi_2$-$NbSi_2$ Pseudobinary Alloys. *Phys. Rev. B* **2012**, *85*, 134106. [CrossRef]
20. Hagihara, K.; Ikenishi, T.; Araki, H.; Nakano, T. Outstanding Compressive Creep Strength in Cr/Ir-Codoped $(Mo_{0.85}Nb_{0.15})Si_2$ Crystals with the Unique Cross-Lamellar Microstructure. *Sci. Rep.* **2017**, *7*, 3936. [CrossRef]
21. Hagihara, K.; Araki, H.; Ikenishi, T.; Nakano, T. Creep-Deformation Behavior of $(Mo_{0.85}Nb_{0.15})Si_2$ Lamellar-Structured C40/$C11_b$ Two-Phase Crystals. *Acta Mater.* **2016**, *107*, 196–212. [CrossRef]
22. Yakaboylu, G.A.; Sabolsky, K.; Sabolsky, E.M. Phase Stability, Microstructure and High-Temperature Properties of $NbSi_2$- and $TaSi_2$-Oxide Conducting Ceramic Composites. *J. Mater. Sci.* **2018**, *53*, 9958–9977. [CrossRef]
23. Zhang, F.; Zhang, L.T.; Shan, A.D.; Wu, J.S. Microstructural Effect on Oxidation Kinetics of $NbSi_2$ at 1023K. *J. Alloys Compd.* **2006**, *422*, 308–312. [CrossRef]
24. Nakano, T.; Hagihara, K.; Nakai, Y.; Umakoshi, Y. Plastic Deformation Behavior of $NbSi_2$/$MoSi_2$ Crystals with Oriented Lamellae. *Intermetallics* **2006**, *14*, 1345–1350. [CrossRef]
25. Umakoshi, Y.; Nakano, T.; Yanagisawa, E.; Takezoe, T.; Negishi, A. Effect of Alloying Elements on Anomalous Strengthening of $NbSi_2$-Based Silicides with C40 Structure. *Mater. Sci. Eng. A* **1997**, *239–240*, 102–108. [CrossRef]
26. Nakano, T.; Azuma, M.; Umakoshi, Y. Microstructure and High-Temperature Strength in $MoSi_2NbSi_2$ Duplex Silicides. *Intermetallics* **1998**, *6*, 715–722. [CrossRef]
27. Umakoshi, Y.; Nakano, T.; Kishimoto, K.; Furuta, D.; Hagihara, K.; Azuma, M. Strength and Deformation Mechanism of C40-Based Single Crystal and Polycrystalline Silicides. *Mater. Sci. Eng. A* **1999**, *261*, 113–121. [CrossRef]
28. Nakano, T.; Nakai, Y.; Maeda, S.; Umakoshi, Y. Microstructure of Duplex-Phase $NbSi_2$(C40)/$MoSi_2$($C11_b$) Crystals Containing a Single Set of Lamellae. *Acta Mater.* **2002**, *50*, 1781–1795. [CrossRef]

29. Hagihara, K.; Nakano, T. Fracture Behavior and Toughness of $NbSi_2$-Based Single Crystals and $MoSi_2(C11_b)/NbSi_2(C40)$ Duplex Crystals with a Single Set of Lamellae. *Acta Mater.* **2011**, *59*, 4168–4176. [CrossRef]
30. Hagihara, K.; Maeda, S.; Nakano, T.; Umakoshi, Y. Indentation Fracture Behavior of $(Mo_{0.85}Nb_{0.15})Si_2$ Crystals with C40 Single-Phase and $MoSi_2(C11_b)/NbSi_2(C40)$ Duplex-Phase with Oriented Lamellae. *Sci. Technol. Adv. Mater.* **2004**, *5*, 11–17. [CrossRef]
31. Zhu, O.; Zhang, L.T.; Yu, J.X.; Shan, A.D.; Wu, J.S.; Nakano, T. Formation and Development of $C40/C11_b$ Lamellar Structure in $NbSi_2/MoSi_2$ Crystals. *Intermetallics* **2010**, *18*, 2328–2332. [CrossRef]
32. Nakano, T.; Kishimoto, M.; Furuta, D.; Umakoshi, Y. Effect of Substitutational Elements on Plastic Deformation Behaviour of $NbSi_2$-Based Silicide Single Crystals with C40 Structure. *Acta Mater.* **2000**, *48*, 3465–3475. [CrossRef]
33. Stoloff, N.S. An Overview of Powder Processing of Silicides and Their Composites. *Mater. Sci. Eng. A* **1999**, *261*, 169–180. [CrossRef]
34. Hu, Q.; Luo, P.; Yan, Y.; Li, J. Microstructure Evolution and Wear Properties of Bulk $MoSi_2$ Fabricated by Field Activated Sintering. *Int. J. Refract. Met. Hard Mater.* **2011**, *29*, 470–477. [CrossRef]
35. Titov, D.D.; Miloserdov, P.A.; Lysenkov, A.S.; Frolova, M.G.; Gumennikova, E.A.; Kargin, Y.F. Rheological Properties of $MoSi_2$-$NbSi_2$ Powders Obtained by SHS-Method and Solid-Phase Mixture. *IOP Conf. Ser. Mater. Sci. Eng.* **2019**, *525*, 012077. [CrossRef]
36. Gorshkov, V.A.; Yukhvid, V.I.; Miloserdov, P.A.; Sachkova, N.V.; Kovalev, D.Y. Cast Silicides of Molybdenum, Tungsten, and Niobium by Combustion Synthesis. *Int. J. Self-Propagating High-Temp. Synth.* **2011**, *20*, 100–106. [CrossRef]
37. Mistler, R.E.; Twiname, E.R. *Tape Casting: Theory and Practice*; American Ceramic Society: Westerville, OH, USA, 2000; ISBN 978-1-57498-029-5.
38. Mukherjee, A.; Maiti, B.; Das Sharma, A.; Basu, R.N.; Maiti, H.S. Correlation between Slurry Rheology, Green Density and Sintered Density of Tape Cast Yttria Stabilised Zirconia. *Ceram. Int.* **2001**, *27*, 731–739. [CrossRef]
39. Hallebrand, H. Processing of Ceramics. 2. In *Tape Casting*; Materials Science and Technology; Cahn, R.W., Ed.; Wiley: Hoboken, NJ, USA, 1996; Volume 17, ISBN 978-3-527-29356-8.
40. Biamino, S.; Liedtke, V.; Badini, C.; Euchberger, G.; Huertas Olivares, I.; Pavese, M.; Fino, P. Multilayer SiC for Thermal Protection System of Space Vehicles: Manufacturing and Testing under Simulated Re-Entry Conditions. *J. Eur. Ceram. Soc.* **2008**, *28*, 2791–2800. [CrossRef]
41. Yang, W.S.; Biamino, S.; Padovano, E.; Fuso, L.; Pavese, M.; Marchisio, S.; Vasquez, D.; Vega Bolivar, C.; Fino, P.; Badini, C. Microstructure and Mechanical Properties of Short Carbon Fibre/SiC Multilayer Composites Prepared by Tape Casting. *Compos. Sci. Technol.* **2012**, *72*, 675–680. [CrossRef]
42. Blanks, K.S.; Kristoffersson, A.; Carlström, E.; Clegg, W.J. Crack Deflection in Ceramic Laminates Using Porous Interlayers. *J. Eur. Ceram. Soc.* **1998**, *18*, 1945–1951. [CrossRef]
43. Zhang, G.-J.; Yue, X.-M.; Watanabe, T. $Al_2O_3/TiC/(MoSi_2+Mo_2B_5)$ Multilayer Composites Prepared by Tape Casting. *J. Eur. Ceram. Soc.* **1999**, *19*, 2111–2116. [CrossRef]
44. Tuffé, S.; Wilkinson, D.S. $MoSi_2$-Based Sandwich Composite Made by Tape Casting. *J. Am. Ceram. Soc.* **1995**, *78*, 2967–2972. [CrossRef]
45. Dumont, A.-L.; Bonnet, J.-P.; Chartier, T.; Ferreira, J.M.F. $MoSi_2/Al_2O_3$ FGM: Elaboration by Tape Casting and SHS. *J. Eur. Ceram. Soc.* **2001**, *21*, 2353–2360. [CrossRef]
46. Roncari, E.; Pinasco, P.; Nagliati, M.; Sciti, D. Tape Casting of AlN–SiC–$MoSi_2$ Composites. *J. Eur. Ceram. Soc.* **2004**, *24*, 2303–2311. [CrossRef]
47. Chen, F.; Xu, J.; Hou, Z. In Situ Pressureless Sintering of $SiC/MoSi_2$ Composites. *Ceram. Int.* **2012**, *38*, 2767–2772. [CrossRef]
48. Jo, H.-G.; Shon, I.-J. Pulsed Current Activated Synthesis and Consolidation of Nanostructured $MoSi_2$–$NbSi_2$ Composite and Its Mechanical Properties. *Mater. Trans.* **2014**, *55*, 391–394. [CrossRef]
49. Kang, H.-S.; Shon, I.-J. Simultaneous Synthesis and Consolidation of Nanostructured $MoSi_2$-$NbSi_2$ Composite by High-Frequency Induction Heated Sintering and Its Mechanical Properties. *Kor. J. Mater. Res.* **2014**, *24*, 180–185. [CrossRef]
50. Zhang, Y.; Zhang, H.; Wu, H.; Gu, S.; Chen, Y. Properties of $CNTs/MoSi_2$ Composites Prepared by Spark Plasma Sintering. *J. Cent. South Univ.* **2016**, *23*, 3060–3064. [CrossRef]
51. Nazari, M.; Shakeri, E.; Mohammadi, M. Fabrication and Optimization Process of Mechanical Properties of $MoSi_2$ Composites Reinforced by Carbon Nanotubes (CNT) Using Taguchi Method. *Ceram. Int.* **2024**, *50*, 25568–25577. [CrossRef]
52. Zhang, L.; Tong, Z.; He, R.; Xie, C.; Bai, X.; Yang, Y.; Fang, D. Key Issues of $MoSi_2$-UHTC Ceramics for Ultra High Temperature Heating Element Applications: Mechanical, Electrical, Oxidation and Thermal Shock Behaviors. *J. Alloys Compd.* **2019**, *780*, 156–163. [CrossRef]
53. Wick-Joliat, R.; Mauchle, S.; Kontic, R.; Ehrat, S.; Hocker, T.; Penner, D. $MoSi_2/Al_2O_3$/Feldspar Composites for Injection-Molded Ceramic Heating Elements. *Adv. Eng. Mater.* **2021**, *23*, 2100517. [CrossRef]
54. Feng, L.; Guan, P.; Yu, X.; He, Y. Microstructure and Properties of Thermal Electrode Material Si_3N_4–$MoSi_2$ Composite Ceramics. *Materials* **2018**, *11*, 986. [CrossRef]

55. Titov, D.D.; Lysenkov, A.S.; Kargin, Y.F.; Gorshkov, V.A.; Goldberg, M.A.; Petrakova, N.V. Low-Temperature Oxidation of $MoSi_2$–Si_3N_4 Composites. *Inorg. Mater. Appl. Res.* **2016**, *7*, 624–629. [CrossRef]
56. Demir, B. Novel $MoSi_2$-MoB_2 Composites: Single-Step in-Situ Synthesis from Elemental Powders via Spark Plasma Sintering. *J. Alloys Compd.* **2026**, *1050*, 185651. [CrossRef]
57. Huang, J.-B.; Zhang, G.-H. Microstructures and Performances of Pressureless Sintered $MoSi_2$-Al_2O_3 Composites. *Corros. Sci.* **2023**, *224*, 111514. [CrossRef]
58. Bei, X.-A.; Zhang, G.-H. Microstructures and High-Temperature Oxidation Behavior of $MoSi_2$-MoAlB Composites. *Corros. Sci.* **2026**, *261*, 113639. [CrossRef]
59. Gao, P.; Xu, M.; Yuan, Z.; Cheng, L.; Liang, J.; Xiao, H.; Chen, R. Temperature Dependence of the Mechanical and Thermal Expansion Behaviors of $MoSi_2$-RSiC Composites with a Three-Dimensionally (3D) Interpenetrated Network Structure. *J. Alloys Compd.* **2018**, *731*, 1103–1111. [CrossRef]
60. Xie, W.; Gao, P.-Z.; Lv, H.-N.; Xu, M.-Y.; Li, D.-Y.; Guo, W.-M.; Xiao, H.-N. Mechanical and Electrical Properties of $MoSi_2$–RSiC Composites via a Combination of Phenolic Resin Infiltration–Pyrolysis and $MoSi_2$–Si–Ti Alloy-Activated Melting Infiltration Composite Processes. *Adv. Appl. Ceram.* **2016**, *115*, 249–259. [CrossRef]
61. Huang, M.; Wang, Q.; Li, S.; Chen, L.; Xiao, H.; Su, X. Dense SiCf/$MoSi_2$ Composite via Liquid Silicon Infiltration. *J. Am. Ceram. Soc.* **2019**, *102*, 5716–5724. [CrossRef]
62. Zhang, X.L.; Xu, J.; Li, S.X.; Fan, J.W.; Jiang, Z.Q.; Fan, W.J.; Yang, J.L. In-Situ Preparation of Nano $MoSi_2$SiC Composite by Melt Infiltration of Silicon Method. *Mater. Chem. Phys.* **2017**, *200*, 287–294. [CrossRef]
63. Jain, M.K.; Das, J.; J., S.; Ray, S. Interfacial Characterization in Ductile Refractory Metals Reinforced $MoSi_2$ Based Laminated Composites. *Int. J. Refract. Met. Hard Mater.* **2017**, *66*, 258–270. [CrossRef]
64. Kaledin, A.; Shikunov, S.; Zubareva, J.; Shmytko, I.; Straumal, B.; Kurlov, V. Fabrication of Layered SiC/C/Si/$MeSi_2$/Me Ceramic–Metal Composites via Liquid Silicon Infiltration of Metal–Carbon Matrices. *Materials* **2024**, *17*, 650. [CrossRef] [PubMed]
65. Lu, Q.; Chen, X.; Fan, J.L. Effect of Nb–Al–SiC Elements Combined with Pre-Oxidation Treatment on the Pesting Resistance of $MoSi_2$. *Ceram. Int.* **2019**, *45*, 15807–15814. [CrossRef]
66. Lu, Q.; Zhu, G.; Wang, X.; Wang, Z.; Feng, P. Effects of Raw Materials on Synthesis, Microstructure and Properties of $MoSi_2$-10 Vol% SiC Composites. *Trans. Indian Ceram. Soc.* **2016**, *75*, 33–39. [CrossRef]
67. Monteverde, F.; Melandri, C.; Failla, S.; Grohsmeyer, R.J.; Hilmas, G.E.; Fahrenholtz, W.G. Escape from the Strength-to-Toughness Paradox: Bulk Ceramics through Dual Composite Architectures. *J. Eur. Ceram. Soc.* **2018**, *38*, 2961–2970. [CrossRef]
68. Pogozhev, Y.S.; Lemesheva, M.V.; Potanin, A.Y.; Vershinnikov, V.I.; Levashov, E.A. Features of the Synthesis and Consolidation of Me^{IV} B_2–(Me^{IV}, Mo)Si_2 Ceramic Powder for High-Temperature Applications. *IOP Conf. Ser. Mater. Sci. Eng.* **2019**, *558*, 012033. [CrossRef]
69. Gorshkov, V.A.; Miloserdov, P.A.; Titov, D.D.; Yukhvid, V.I.; Kargin, Y.F. SHS Metallurgy of Binary Silicides (MoW)Si_2 for Sintering Composite Materials. *Inorg. Mater. Appl. Res.* **2019**, *10*, 473–479. [CrossRef]
70. Yeh, C.-L.; Peng, J.-A. Combustion Synthesis of $MoSi_2$-Al_2O_3 Composites from Thermite-Based Reagents. *Metals* **2016**, *6*, 235. [CrossRef]
71. Zaki, Z.I.; Mostafa, N.Y.; Ahmed, Y.M.Z. Synthesis of Dense Mullite/$MoSi_2$ Composite for High Temperature Applications. *Int. J. Refract. Met. Hard Mater.* **2014**, *45*, 23–30. [CrossRef]
72. Potanin, A.Y.; Vorotilo, S.; Pogozhev, Y.S.; Rupasov, S.I.; Lobova, T.A.; Levashov, E.A. Influence of Mechanical Activation of Reactive Mixtures on the Microstructure and Properties of SHS-Ceramics $MoSi_2$–HfB_2–MoB. *Ceram. Int.* **2019**, *45*, 20354–20361. [CrossRef]
73. Vorotilo, S.; Potanin, A.Y.; Pogozhev, Y.S.; Levashov, E.A.; Kochetov, N.A.; Kovalev, D.Y. Self-Propagating High-Temperature Synthesis of Advanced Ceramics $MoSi_2$–HfB_2–MoB. *Ceram. Int.* **2019**, *45*, 96–107. [CrossRef]
74. Vorotilo, S.; Potanin, A.Y.; Iatsyuk, I.V.; Levashov, E.A. SHS of Silicon-Based Ceramics for the High-Temperature Applications. *Adv. Eng. Mater.* **2018**, *20*, 1800200. [CrossRef]
75. Yan, J.; Huang, J.; Li, K.; Zhou, P.; Wang, Y.; Qiu, J. Effect of Boron Content on Microstructure, Mechanical Properties, and Oxidation Resistance of Mo-Si-B Composites. *J. Mater. Eng. Perform.* **2018**, *27*, 6218–6226. [CrossRef]
76. Zhang, X.; Zhang, X.; Duan, J.; Lu, K. The Preparation of In-Situ $MoSi_2$-SiC-MoB Three-Phase Composite Completely Eliminating the PEST Phenomena. *Mater. Chem. Phys.* **2019**, *235*, 121730. [CrossRef]
77. Safaie, P.; Haghshenas-Jazi, E.; Borhani, G.H.; Bakhshi, S.R.; Alizadeh, M. In Situ Synthesis of $MOSi_2$-Al_2O_3 Composite by Mechanical Milling and Subsequent Heat Treatment. *Synth. React. Inorg. Met.-Org. Nano-Met. Chem.* **2015**, *45*, 879–884. [CrossRef]
78. Silvestroni, L.; Stricker, K.; Sciti, D.; Kleebe, H.-J. Understanding the Oxidation Behavior of a ZrB_2–$MoSi_2$ Composite at Ultra-High Temperatures. *Acta Mater.* **2018**, *151*, 216–228. [CrossRef]
79. Huang, J.-B.; Zhang, G.-H.; Yang, X.-H. Effect of WSi_2 Content on Oxidation Behavior of $MoSi_2$-20 Vol% Al_2O_3 Composites. *Powder Technol.* **2023**, *430*, 119012. [CrossRef]

80. Hu, D.; Fu, Q.; Liu, B.; Zhou, L.; Sun, J. Multi-Layered Structural Designs of $MoSi_2$/Mullite Anti-Oxidation Coating for SiC-Coated C/C Composites. *Surf. Coat. Technol.* **2021**, *409*, 126901. [CrossRef]
81. Chen, P.; Zhu, L.; Ren, X.; Kang, X.; Wang, X.; Feng, P. Preparation of Oxidation Protective $MoSi_2$–SiC Coating on Graphite Using Recycled Waste $MoSi_2$ by One-Step Spark Plasma Sintering Method. *Ceram. Int.* **2019**, *45*, 22040–22046. [CrossRef]
82. Li, W.; Fan, J.; Fan, Y.; Xiao, L.; Cheng, H. $MoSi_2$/(Mo, Ti)Si_2 Dual-Phase Composite Coating for Oxidation Protection of Molybdenum Alloy. *J. Alloys Compd.* **2018**, *740*, 711–718. [CrossRef]
83. Bezzi, F.; Burgio, F.; Fabbri, P.; Grilli, S.; Magnani, G.; Salernitano, E.; Scafè, M. SiC/$MoSi_2$ Based Coatings for Cf/C Composites by Two Step Pack Cementation. *J. Eur. Ceram. Soc.* **2019**, *39*, 79–84. [CrossRef]
84. Zhu, J.; Su, T.; Lei, S.; Li, F.; Sun, A.; Zhang, X.; Li, W. Oxidation Resistance and Diffusion Behavior of $MoSi_2$-SiCw Composite Coating on Nb Alloy Exposed at Static or Cyclic Oxidation. *Int. J. Refract. Met. Hard Mater.* **2024**, *121*, 106632. [CrossRef]
85. Zhang, W.; Qiao, Y.; Guo, X.; Li, L.; Nan, X. Excellent Oxidation Resistance: A Dense and Well-Bonded $MoSi_2$/(Nb,X)Si_2 Composite Coating on Nb-Si Based Alloy. *Corros. Sci.* **2025**, *249*, 112863. [CrossRef]
86. Ji, X.; Zhao, J.; Ren, X.; Shang, Z.; Ji, C.; Wang, P.; Sun, Y.; Kiryukhantsev-Korneev, P.V.; Levashov, E.A.; Kang, X.; et al. Thermal Expansion Mismatch-Induced in Situ Self-Assembly Design of Gradient Coatings: 1700 °C Oxidation Protection and Oxygen Barrier Enhancement Mechanism of Borosilicate-Modified ZrB_2-$MoSi_2$-BSG Gradient Composite Coatings. *Corros. Sci.* **2026**, *260*, 113581. [CrossRef]
87. Zhai, R.; Liang, Y.; Huang, T.; Ji, Q.; Dong, Q.; Wang, T.; Zhuang, Y.; Bai, J.; Yang, Z.; Song, P. Non-Isothermal Oxidation Kinetics and Mechanism of Whisker Reinforced ZrB_2-SiC-$MoSi_2$ Composite Powder. *Mater. Charact.* **2025**, *225*, 115196. [CrossRef]
88. Pavese, M.; Fino, P.; Ortona, A.; Badini, C. Potential of SiC Multilayer Ceramics for High Temperature Applications in Oxidising Environment. *Ceram. Int.* **2008**, *34*, 197–203. [CrossRef]
89. Padovano, E.; Badini, C.; Biamino, S.; Pavese, M.; Yang, W.S.; Fino, P. Pressureless Sintering of ZrB_2–SiC Composite Laminates Using Boron and Carbon as Sintering Aids. *Adv. Appl. Ceram.* **2013**, *112*, 478–486. [CrossRef]
90. *ASTM C 1259-21*; Test Method for Dynamic Youngs Modulus, Shear Modulus, and Poisson's Ratio for Advanced Ceramics by Impulse Excitation of Vibration. C28 Committee ASTM International: West Conshohocken, PA, USA, 2021. [CrossRef]
91. *UNI EN 658-3:2002*; Advanced Technical Ceramics—Mechanical Properties of Ceramic Composites at Room Temperature—Determination of Flexural Strength. Ente Italiano Normazione: Milano, Italy, 2002.
92. Geng, T.; Li, C.; Bao, J.; Zhao, X.; Du, Z.; Guo, C. Thermodynamic Assessment of the Nb–Si–Ti System. *Intermetallics* **2009**, *17*, 343–357. [CrossRef]
93. Silva, A.C.e.; Kaufman, M.J. Phase Relations in the Mo-Si-C System Relevant to the Processing of $MoSi_2$-SiC Composites. *Metall. Mater. Trans. A* **1994**, *25*, 5–15. [CrossRef]
94. Fleischer, R.L.; Westbrook, J.H. *Intermetallic Compounds: Principles and Practice*; Wiley: Chichester, UK, 1995; ISBN 978-0-471-94219-1.
95. Yaney, D.L.; Joshi, A. Reaction between Niobium and Silicon Carbide at 1373 K. *J. Mater. Res.* **1990**, *5*, 2197–2208. [CrossRef]
96. Boettinger, W.J.; Perepezko, J.H.; Frankwicz, P.S. Application of Ternary Phase Diagrams to the Development of $MoSi_2$-Based Materials. *Mater. Sci. Eng. A* **1992**, *155*, 33–44. [CrossRef]
97. Zhou, P.; Hu, P.; Zhang, X.; Han, W. Laminated ZrB_2–SiC Ceramic with Improved Strength and Toughness. *Scr. Mater.* **2011**, *64*, 276–279. [CrossRef]
98. Wu, J.; Wang, W.; Zhou, C. Microstructure and Oxidation Resistance of Mo–Si–B Coating on Nb Based in Situ Composites. *Corros. Sci.* **2014**, *87*, 421–426. [CrossRef]
99. Song, B.; Feng, P.; Wang, J.; Ge, Y.; Wu, G.; Wang, X.; Akhtar, F. Oxidation Properties of Self-Propagating High Temperature Synthesized Niobium Disilicide. *Corros. Sci.* **2014**, *85*, 311–317. [CrossRef]
100. Majumdar, S.; Kishor, J.; Paul, B.; Hubli, R.C.; Chakravartty, J.K. Isothermal Oxidation Behavior and Growth Kinetics of Silicide Coatings Formed on Nb–1Zr–0.1C Alloy. *Corros. Sci.* **2015**, *95*, 100–109. [CrossRef]
101. Chaia, N.; Cury, P.L.; Rodrigues, G.; Coelho, G.C.; Nunes, C.A. Aluminide and Silicide Diffusion Coatings by Pack Cementation for Nb-Ti-Al Alloy. *Surf. Coat. Technol.* **2020**, *389*, 125675. [CrossRef]
102. Fu, T.; Zhan, S.; Zhang, Y.; Shen, F.; Wang, H. Preparation of Si-Rich $NbSi_2$ Coating on Nb Surface by Hot Dip Silicon-Plating Technology to Improve the High-Temperature Oxidation Resistance of Pure Nb Substrate. *Ceram. Int.* **2025**, *51*, 23341–23353. [CrossRef]
103. Zhang, F.; Zhang, L.T.; Shan, A.D.; Wu, J.S. In Situ Observations of the Pest Oxidation Process of $NbSi_2$ at 1023K. *Scr. Mater.* **2005**, *53*, 653–656. [CrossRef]
104. Li, N.; Gao, J.; Wang, W.; Chen, S.-C.; Wang, K.; Wang, Y.; Wen, C.-K.; Sun, H. Oxidation Resistance of Cr-Modified $MoSi_2$ Composites at High Temperature. *Int. J. Refract. Met. Hard Mater.* **2024**, *119*, 106497. [CrossRef]

Disclaimer/Publisher's Note: The statements, opinions and data contained in all publications are solely those of the individual author(s) and contributor(s) and not of MDPI and/or the editor(s). MDPI and/or the editor(s) disclaim responsibility for any injury to people or property resulting from any ideas, methods, instructions or products referred to in the content.